

RESEARCH ARTICLE

10.1029/2018JD028368

Key Points:

- Meiyu precipitation over China show pronounced diurnal cycles including early morning maximum and evening minimum
- The morning maximum and evening minimum are directly linked to maximum low-level moisture convergence and divergence that occur 2–3 hr earlier
- Diurnal variations in the boundary layer winds due to inertial oscillations are primarily responsible for the variations in low-level convergence forcing and precipitation diurnal cycles

Correspondence to:

M. Xue,
mxue@ou.edu

Citation:

Xue, M., Luo, X., Zhu, K., Sun, Z., & Fei, J. (2018). The controlling role of boundary layer inertial oscillations in Meiyu frontal precipitation and its diurnal cycles over China. *Journal of Geophysical Research: Atmospheres*, 123, 5090–5115. <https://doi.org/10.1029/2018JD028368>

Received 22 JAN 2018

Accepted 15 APR 2018

Accepted article online 27 APR 2018

Published online 24 MAY 2018

The Controlling Role of Boundary Layer Inertial Oscillations in Meiyu Frontal Precipitation and Its Diurnal Cycles Over China

Ming Xue^{1,2} , Xia Luo^{1,2,3}, Kefeng Zhu¹ , Zhengqi Sun^{1,2}, and Jianfang Fei³ 

¹School of Atmosphere Sciences, Nanjing University, Nanjing, China, ²Center for Analysis and Prediction of Storms, University of Oklahoma, Norman, OK, USA, ³College of Meteorology and Oceanography, National University of Defense Technology, Nanjing, China

Abstract Convection-permitting simulations are used to investigate the key mechanism of Meiyu precipitation diurnal cycle over China. Six days from the 2014 Meiyu season are used to produce a “north” composite rainband over the Yangtze-Huaihe River Basin and another 6 days used to produce a “south” composite band. Both rainbands have peak rainfall in the early morning, while the south band has a secondary peak in the afternoon. Low-level ageostrophic winds (AGWs) are found to exhibit diurnal cycles with clockwise rotations and their directions, and magnitudes depend on the background geostrophic monsoon flows. Net moisture flux into a control volume enclosing each rainband is almost purely due to AGWs. For both rainbands, net flux reaches maximum at ~04 LST, about 3–4 hr before morning precipitation peak. For the north band, a prominent minimum occurs at ~19 LST, 4 hr before the precipitation minimum. The moisture fluxes through the southern control volume boundary make the largest contributions to the net flux and its diurnal variations. The diurnal variations of the AGWs and their relationship with the background monsoon flows agree very well with the prediction of Blackadar boundary layer inertial oscillation theory, and the convergence forcing by the AGWs resulting from the inertial oscillations plays a paramount role in modulating the diurnal cycles of Meiyu front precipitation, including the creation of early morning peak and evening minimum. Feedback of latent heat release plays only a secondary role. The commonly recognized diurnal monsoon variability can be explained by the Blackadar inertial oscillation theory.

1. Introduction

The Meiyu season over the Yangtze-Huaihe River Basin (YHRB) of China, typically occurring from mid-June to mid-July, is a period with frequent heavy rainfall (Ding, 1992) along the Meiyu frontal rainband. The Meiyu rainband also exhibits large variabilities on time scales ranging from hours to interannual and has a close association with the seasonal advance and retreat of the East Asian summer monsoon (Chang et al., 2000; Ding & Chan, 2005; T. Li et al., 2017; Sampe & Xie, 2010). Gaining a better understanding of the spatial and temporal variabilities of Meiyu precipitation has important implications for improving heavy rainfall prediction and water resource management. In fact, diurnal variations in the amount, frequency, intensity, and regimes of summer season precipitation over contiguous China have received much attention in recent years (Bao et al., 2011; G.-X. Chen et al., 2009a, 2012; X.-C. Chen et al., 2014; W. Xu et al., 2009; Yu & Li, 2016, 2014; Yu, Xu, et al., 2007; Yu, Zhou, et al., 2007; Yuan et al., 2012; Zhou et al., 2008).

One of the most pronounced features of the summer precipitation diurnal cycle is the strong region dependence that results from the combined effect of the large-scale environments and inhomogeneous surface (orography, land-sea contrast, land use and land cover differences, etc.) conditions over the subtropical East Asia (Hirose & Nakamura, 2005; Yu et al., 2014; Yuan et al., 2012). Consider the daily rainfall peak time, for example. The rainfall peaks mainly in the afternoon over southern and northeastern China (Yu, Zhou, et al., 2007), while precipitation peaks at midnight in southwestern China near Sichuan Basin (W. Xu et al., 2009; Yin et al., 2009). Over the eastern China Plains, two comparable diurnal peaks appear in the late afternoon and early morning (He & Zhang, 2010; Yu, Zhou, et al., 2007; Yuan et al., 2012). Over regions with concentrated summer precipitation, such as the upper and middle reaches of the YHRB, most precipitation occurs in the early morning (Yin et al., 2009; Yu, Zhou, et al., 2007). The diurnal cycle of the Meiyu rainband, first explored in Geng and Yamada (2007), also attains such a morning peak, suggesting that morning rainfall may dominate these areas in Meiyu season.

In addition to documenting the observed characteristics of diurnal variations in warm season precipitation over China, efforts have also been made to explore responsible mechanisms and related physics of diurnal variations. The precipitation diurnal modes have been found to be strongly correlated with thermal circulations driven by differential diabatic heating associated with topographic forcing, including regional mountain-plains solenoid (MPS) circulations and land-sea breezes (Bao et al., 2011; Bao & Zhang, 2013; X.-C. Chen et al., 2014; He & Zhang, 2010; Sun & Zhang, 2012). For instance, the eastward propagation of precipitation systems that develop over the Tibetan Plateau (TP) and the solenoidal circulations between TP and its leeside lowlands are believed to modulate the longevity and diurnal variations of summer precipitation over the regions downstream of TP (G.-X. Chen et al., 2012; Huang et al., 2010; C. C. Wang et al., 2004). Studies have also suggested that nighttime cloud top radiative cooling could be the process behind the nocturnal rain in the western part of China (Yin et al., 2009).

The prevailing synoptic-scale, southwesterly low-level flows coupled with active monsoon systems have long been recognized as crucial factors for maintaining the rainfall along the YRHB (Ding et al., 2001; W.-C. Wang et al., 2000). The close relationship between the low-level southwesterly jet and heavy precipitation over the East Asia has been well recognized (G. T.-J. Chen et al., 2005; G. T.-J. Chen & Yu, 1988). These earlier studies mainly focused on synoptic scale low-level jets (LLJs) which have their peak speed between 850 and 700 hPa levels. In studies for the Taiwan region, frequent occurrence of LLJs below 900 hPa had been documented that were attributed to the blocking effect of the Central Mountain Range of Taiwan (G. T.-J. Chen et al., 2005; J. Li & Chen, 1998). The synoptic LLJs generally do not explain the diurnal cycles of precipitation.

The important role of nocturnal LLJ in affecting the diurnal cycle of rainfall has long been recognized over the Great Plains of the United States (Bonner, 1966; Carbone & Tuttle, 2008; Helfand & Schubert, 1995; Trier et al., 2014; Tuttle & Davis, 2006; Wallace, 1975; Zhong et al., 1996). The primary mechanisms of the Great Plains LLJ include the initial oscillation mechanism of Blackadar (1957) associated with the diurnal variation of surface frictional effect on the boundary layer, and the thermal wind adjustment mechanism in response to diurnal change in the pressure gradient force due to the heating and cooling of sloped terrains (Holton, 1967). Based on the initial oscillation mechanism of Blackadar, diurnally oscillating ageostrophic wind vector would rotate clockwise with time at a period of $2\pi/f$ where f is the Coriolis parameter in idealized conditions (Blackadar, 1957; Markowski & Richardson, 2010). In general, the Blackadar inertial oscillation theory explains better the behaviors of the Great Plains LLJ than the Holton theory, although most recently a unified theory has been proposed that combines the two effects (Shapiro et al., 2016), resulting in a better fit of the theoretical prediction to observations. In comparison, the boundary layer LLJ and its diurnal oscillations over China have been studied less, with Du and Zhang (2012); Du et al. (2014); Du, Chen, and Zhang (2015); and Du, Rotunno, and Zhang (2015) being some of the few examples. These studies also suggest that inertial oscillations play important roles.

During the warm season of China, the onset of southerly or southwesterly summer monsoon sets up strong low-level flows, often in the form of strong synoptic-scale LLJ (Du et al., 2014). Such a condition is favorable for strong boundary layer LLJ, as the amplitude of inertial oscillations is proportional to the geostrophic wind speed (Blackadar, 1957; Klein et al., 2016). In a climatological study examining the relation between rainfall duration and diurnal variation in the warm season precipitation over central eastern China, Yu et al. (2009) noticed that the winds at surface stations located on the top of mountains (of about 1- to 1.5-km height MSL) showed distinct diurnal variations, and the winds at those stations were strongest predawn and weakest in the afternoon. The daily wind anomaly also rotated clockwise from late night to late afternoon, "similar to the diurnal variation of the troposphere low-level wind." While the potential linkage of such lower tropospheric wind variations to diurnal precipitation variations was recognized, no clear explanation was offered on the cause of the diurnal variations of wind speed and direction in Yu et al. (2009) nor did other related studies (e.g., G.-X. Chen et al., 2009a; H. Chen et al., 2010). In G.-X. Chen et al. (2009a), the low-level winds over southern China was found to be strongest at late night or in early morning, and they referred to this diurnal change as diurnal monsoon variability (DMV). They did point out that the DMV was related closely to ageostrophic wind component and suggested that the clockwise rotation of wind vector at night was probably a response to the inertial oscillation, with reference to Blackadar (1957). The relationship between DMV and Meiyu frontal rainfall was further documented in G.-X. Chen et al. (2009b), although no clear explanation on the cause of the DMV was given.

In Sun and Zhang (2012), the upward branch of the nighttime thermally driven MPS circulation over the plains east of the TP was believed to be primarily responsible for the midnight-to-early-morning rainfall enhancement along the Meiyu front, while daytime downward circulation acted to suppress convection over the plains, although enhanced nocturnal LLJ was also suggested to be a possibly important contributor. Sun and Zhang (2012) also suggested that future studies should be conducted to investigate the mechanisms of LLJ diurnal variations and their impacts on diurnal cycle of precipitation over China. In a most recent study (G.-X. Chen et al., 2017), the role of nocturnal LLJ in modulating mesoscale convective systems (MCSs) and associated heavy rainfall along a Meiyu front was emphasized much more, based on a study on a 5-day period in June 1998 when moist convection repeatedly occurred in the midnight-to-morning hours causing severe flooding. Their study found that “a train of MCSs concurrently developed along a quasi-stationary Meiyu front and coincided with the impact of a monsoon surge on a frontogenetic zone at night. This process was regulated primarily by a nocturnal low-level jet (NLLJ) in the southwesterly monsoon that formed over southern China and extended to central China.” The lifting and destabilization by the convergence at northern terminus of the LLJ was found to be much stronger than free atmospheric forcing. Their study suggests that the MPS circulation forcing likely played a much smaller role than the LLJ forcing, for their period of study at least.

It is clear that the most important factor causing the distinct diurnal cycles of Meiyu front precipitation is still not entirely clear; in fact, it is still a matter of debate. In this study, we utilize WRF model forecast data sets from the Meiyu season of 2014 that were produced in real time at a 4-km grid spacing over the entire continental China (Zhu et al., 2018) and investigate the primary forcing mechanism for the pronounced diurnal cycles of precipitation associated with the Meiyu front. Zhu et al. (2018) show that the seasonal migration of the precipitation zones and the spatial distribution and propagation of precipitation systems, as well as the diurnal cycles of precipitation, were well reproduced by the 4-km WRF model. In this study, specific focus is placed on the diurnal cycles of precipitation during the Meiyu season of 2014, when the main Meiyu rainband was located over the YHRB, and during days when the Meiyu rainband was located further south over southern China. Composite data sets for cases located over the two general regions are created through case averaging, and the flow fields are decomposed into geostrophic and ageostrophic components, and the behaviors of the two wind components are examined. The boundary layer flows are found to exhibit clear clockwise rotation, indicative boundary layer inertial oscillations. Budget analyses of low-level moisture convergence into the Meiyu rainband region show close and time-delayed correlation between the boundary layer moisture convergence due to ageostrophic winds and the Meiyu front precipitation.

The rest of this paper is organized as follows: the observational data used, the model prediction data set and the model configurations, and the method for separating ageostrophic and geostrophic flows are introduced in section 2. Section 3 discusses the selection of Meiyu precipitation dates and the grouping of the dates based on the Meiyu rainband location. It also presents the general characteristics of composite rainbands. Diurnal variations of low-level winds and moisture fluxes, the influences of the boundary layer inertial oscillations, and the feedback effect of the latent heating on the Meiyu rainband diurnal cycles are discussed in section 4, together with a proposed conceptual model. Summary and conclusions are given in section 5.

2. Data Set, Model Configurations, and Filtering Method

2.1. Observational Data

The operational hourly rainfall data from the China Meteorological Administration are first used to validate the precipitation forecasts. The data sets contain over 30,000 sites across China and most of them are automated weather stations (Luo et al., 2013; Pan et al., 2012) and are most densely distributed over the eastern and southern parts of China. The distribution of the stations within our study domain is shown in Figure 1, together with a Meiyu front for illustrative purpose. A quality control procedure that consists of commonly used temporal and spatial consistency and extreme value checks is applied to the hourly rainfall reports, as was described in Zhu et al. (2018). Given that the mean station spacing in the study area is 7–8 km, the resolution of the data is considered excellent.

2.2. Numerical Model Configurations

The primary model data set used in this study is from experimental real-time WRF-ARW model (Powers et al., 2017; Skamarock et al., 2005) forecasts that cover the entire continental China. These forecasts were

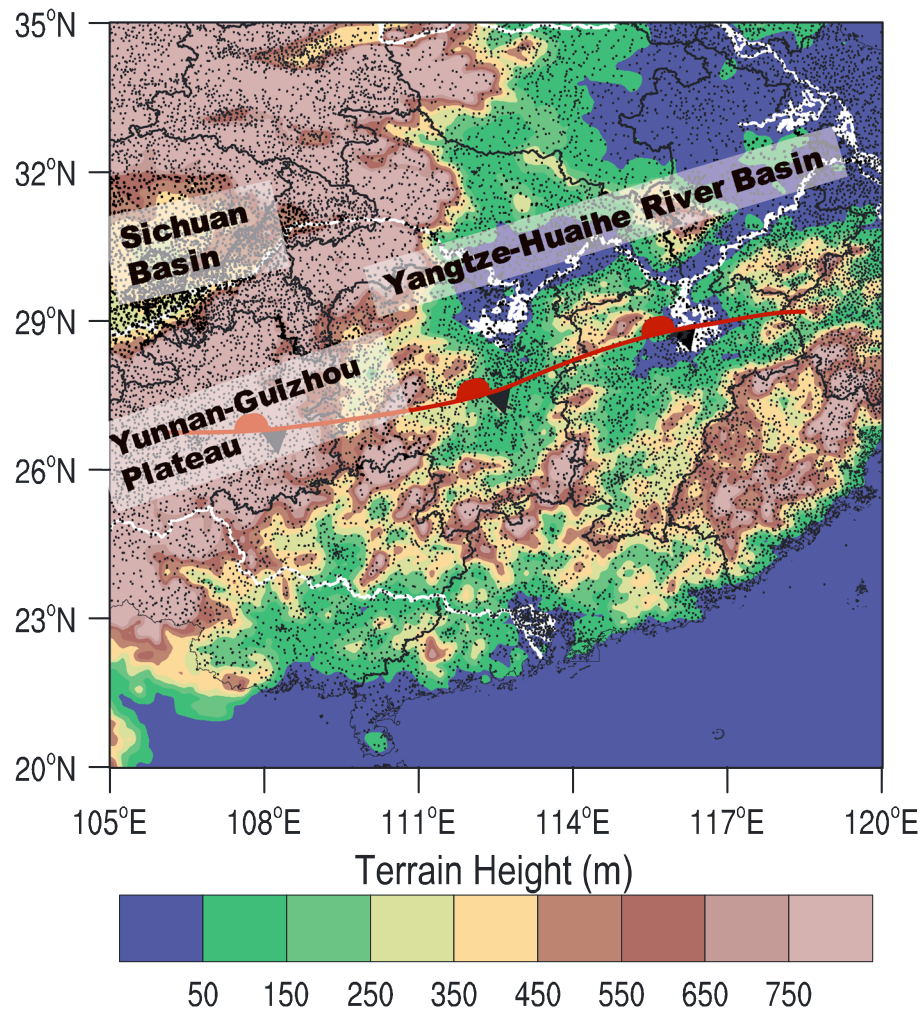


Figure 1. The model domain with terrain height (m) shaded. The densely distributed automated weather stations with rain gauge data are marked as black dots. The Meiyu front in its general location during the study period is shown using standard symbol, together with the Yangtze River which is drawn as thick white lines.

produced twice a day from 00 and 12 UTC (LST = UTC + 8) at 4-km grid spacing and run for 48 hr during the summer months of June through August since 2013 at Nanjing University. The effort was part of the Observation, Prediction, and Analysis of severe Convection of China Project (Xue, 2016). The forecasts from 2013 and 2014 are systematically evaluated in Zhu et al. (2018), and those from 2014 are used in this study.

The model domain had $1,409 \times 1,081$ horizontal grid points and 51 levels in the vertical direction and was centered at 36°N , 105°E . The initial and lateral boundary conditions were, respectively, the operational U.S. National Centers for Environmental Prediction Global Forecasting System (Yang et al., 2006) analyses and forecasts on a 0.5° horizontal resolution grid with 27 vertical levels, with the forecasts available at 3-h intervals. The Morrison double-moment microphysics (Morrison et al., 2009), the ACM2 boundary layer parameterization (Pleim, 2007), the Pleim-Xiu land surface model (Pleim & Xiu, 1995), and the CAM short and long radiation schemes were employed in the forecasts. No cumulus parameterization was used. More details can be found in Zhu et al. (2018).

The forecasts starting from 00 and 12 UTC have roughly comparable prediction skills, and in this study only the 12 UTC forecasts are used. As shown in Zhu et al. (2018), in the first 6 hr of forecast, the precipitation forecast skill is poor because of the model spin-up but after 6 hr, the predicted mean hourly precipitation shows a good match of the diurnal cycle to observations, with a slight overprediction in the amplitude, mostly in the afternoon. To avoid the initial spin-up period, 12- to 36-hr forecasts are used to produce composites of 24-hr forecasts and to investigate the diurnal cycle issues.

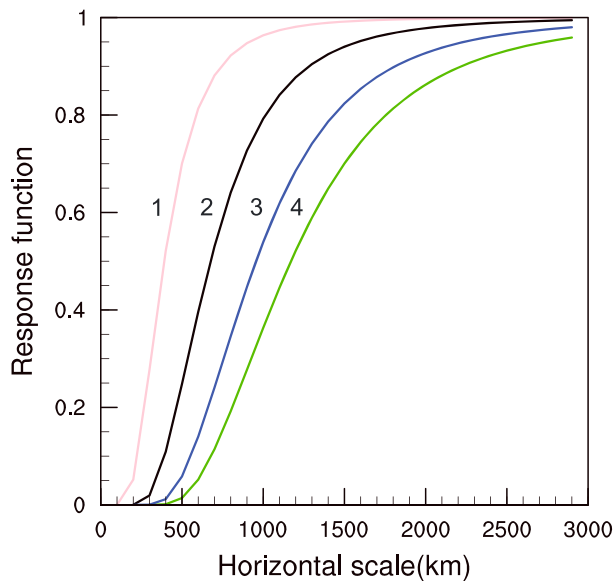


Figure 2. Response function of large-scale low-pass filters following Barnes (1964). Lines of different colors indicate different response amplitudes which are determined by weight function constants.

2.3. Filtering Method

Previous studies have examined deviations of the total wind from daily mean to identify diurnal cycles in the wind fields (G.-X. Chen et al., 2013; X.-C. Chen et al., 2015; Sun & Zhang, 2012). In this study, we choose to separate the ageostrophic component of winds from the geostrophic component; in the Blackadar inertial oscillation theory it is the ageostrophic wind that oscillates and rotates clockwise around the geostrophic wind vector. It is also the ageostrophic wind that contributes to horizontal convergence and hence low-level lifting forcing as geostrophic flow is mostly nondivergent.

We obtain the geostrophic winds from the geopotential height field that is first smoothed by applying a low-pass Barnes filter that was designed as part of an objective analysis scheme (Barnes, 1964; Koch et al., 1983). Some details on the filter, including the response function for given wavelength λ , can be found in Appendix A. X. Xu et al. (2017) is an example use of the filter to separate flows into the synoptic, mesoscale and convective scale. Without the filtering, the geostrophic winds calculated from the unfiltered pressure fields are noisy.

Using $g = 0.3$ (values less than 0.5 are recommended by Koch et al., 1983), the response functions for parameter $c = 10,000; 30,000; 60,000;$ and $90,000$ are plotted in Figure 2 as lines 1, 2, 3, and 4, respectively.

It can be seen that for line 2, waves with 1,000-km wavelength is damped by nearly 20% and waves of 500-km wavelength is damped by about 70%. By using $g = 0.3$ and $c = 30,000$, waves shorter than 500 km are mostly damped while waves longer than 1,000 km are mostly retained, so that ageostrophic scales are mostly damped, leaving mostly geostrophic scales. We therefore choose to use these two parameter values.

The geostrophic wind components u_g and v_g are then computed from the filtered geopotential height fields. The Coriolis parameter takes its local value in the calculations. The ageostrophic wind vector V_a is obtained by subtracting the geostrophic wind from total wind: $V_a = V - V_g$.

3. General Characteristics of the Meiyu Frontal Precipitation

3.1. Selected Dates of Meiyu Frontal Precipitation

As discussed in Zhu et al. (2018), the summer (June–August) season precipitation of 2014 was biased toward southern part of China, compared to more typical years. Because of the focus of this study is on the mean diurnal behaviors of Meiyu frontal rainband precipitation over a number of similar cases, we want to restrict our selection of cases whose rainband was located at more or less similar locations, to avoid smearing of features by the composite averaging process. According to China Meteorological Administration, the YHRB Meiyu season of 2014 started on 14 June and ended on 11 July. During the season, 12 (nonconsecutive) days had clearly identifiable Meiyu rainband without direct impact by any tropical cyclone or cold front. Among the 12 days, on 18, 19, 20, 21, 27, and 28 June, the Meiyu rainband was at more southern locations within the 23°N and 30°N latitudinal zone (between southern China and YHRB), and on 25, 26, 29, and 30 June and 1 and 2 July, the rainband was located further north within the 26°N and 32°N latitudinal zone in the YHRB region. It is clear that the days in the first group are mostly from the early half of the Meiyu period, while those in the second group at more northern locations are mostly from the second half, when the Meiyu front migrated further north. Between 25 and 28 June, there were oscillations in the Meiyu front location. The two latitudinal zones have certain width and have some overlap, because there were diurnal changes in the Meiyu rainband locations. The rainband had generally a west-southwest to east-northeast orientation (see Figure 4 later). Therefore, within the officially defined YHRB Meiyu season, the Meiyu rainband showed a northward jump in its location by about 3° in latitude.

The two groups of days are used to produce two composite rainbands, referred to as the south and north rainband, respectively. As will be shown later, compared to observations, the average characteristics of the

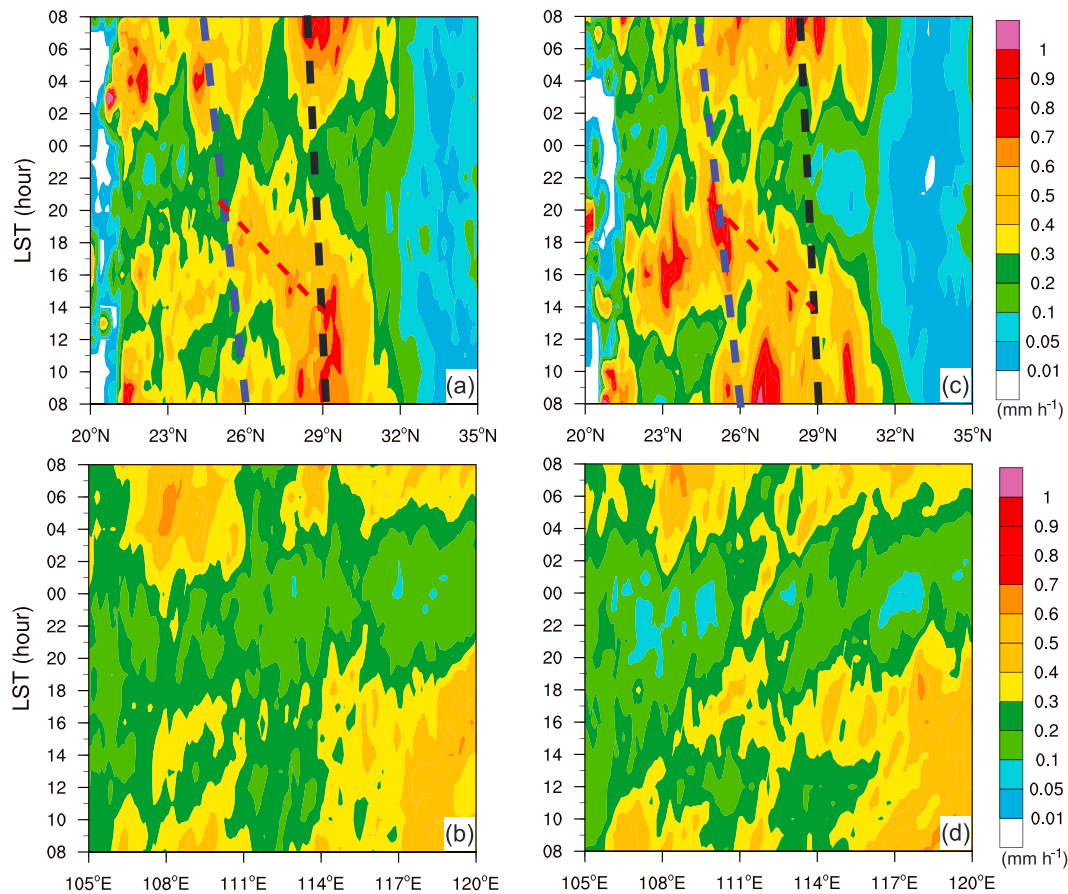


Figure 3. (a) Latitude-time Hovmöller diagram of rain rate averaged over 105°–120°E (see Figure 1) and (b) longitude-time Hovmöller diagram of rain rate averaged over 20°–35°N derived from observations, corresponding to all 12 days of WRF forecasts used in this study. (c) and (d) correspond to (a) and (b) respectively but for WRF simulations. Blue and black dashed lines in (a) and (b) roughly indicate the south and north rainbands, respectively.

rainbands, including their diurnal cycles and propagation, are fairly well captured by the model, except for some location and intensity biases.

3.2. Distributions and Diurnal Cycles of Precipitation Bands

To get a general idea on the diurnal variations and locations of the Meiyu rainband over the 12 chosen days, we plot in Figure 3 the latitude-time and longitude-time Hovmöller diagrams for precipitation within the 20°–35°N and 105°–120°E domain (see Figure 1 for a geographic map). From the latitude-time diagram, we see a tendency of southward propagation of precipitation between 14 and 22 LST from 28°N to 25°N in the observations, as indicated the negative tilt of the red dashed line along the heavy precipitation with time (Figure 3a). Generally, even at the latitudes of primary rainband between 27°N and 30°N, the precipitation between 20 and 02 LST is very weak. Precipitation is the strongest in the early morning hours around 08 LST (Figure 3a). There is a hint of secondary maximum in the precipitation in the 23°N–27°N latitudinal zone, corresponding to the southern locations of rainband mentioned earlier. In the WRF forecasts (Figure 3c), the two latitudinal zones of heavier precipitation are reproduced reasonably well, together with the trend of southward propagation in the afternoon, although there are clear biases in the predicted intensity and location of precipitation. The southward propagation of rainband in the afternoon hours could be caused by the weakening of southerly monsoon flows in the boundary layer due to boundary layer mixing, and the buildup of cold pools from the peak early morning precipitation. The imbalance between the cold pool and northward monsoon flow causes the gust front and the associated precipitation band to advance southward. In Figures 3a and 3c, we also notice a precipitation maximum at around 23°N in the afternoon hours between 13 and 18 LST, with that in the WRF forecasts being stronger. Such precipitation is clearly due to

afternoon surface heating, which tends to trigger convection more easily at the lower latitudes in southern China. Zhu et al. (2018) pointed out that the overprediction of afternoon convective precipitation was the most noticeable forecast deficiency in the WRF 4-km real-time forecasts used here, although the afternoon peak is definitely found in the observations also.

In the longitude-time Hovmöller diagram (Figures 3b and 3d), the most pronounced feature seen is the precipitation maximum in the early morning hours, which starts earlier shortly after 00 LST and reaches maximum between 04 and 06 LST in the western part of the domain (between 106°E and 110°E) and occurs later after 04 LST and reaches maximum around 08 LST over the eastern part (between 112° and 120°E); such an east-west phase difference of diurnal precipitation cycles is still a topic of debate (H. Chen et al., 2010; G.-X. Chen et al., 2017) and is not a focus of this study. Generally, the earlier occurrence of nighttime precipitation in the western part of the domain should be related to the major terrains including the Tibetan and Yunnan-Guizhou Plateaus and Sichuan Basin (cf. Figure 1).

Apart from the precipitation peak in the early morning hours, the secondary peak in the afternoon is also evident in both observations (Figure 3b) and WRF forecasts (Figure 3d); with the model peak being stronger and delayed by a couple of hours. Ignoring the afternoon thermal convection, precipitation starts to weaken significantly after 10 LST west of 114°E and does not regain strength until after midnight. East of 117°E, the morning precipitation peak is maintained through the afternoon until after 18 LST, presumably aided by rich moisture supply in the southern and eastern China regions. The minimum is found in the evening through midnight, with some phase delay going eastward. There are also some streaks of precipitation (e.g., that between 109°E and 112°E and between 16 and 02 LST) that indicate eastward propagation at roughly 8 m/s; these are most likely due to eastward propagation of MCSs along the Meiyu front. Signs of eastward propagation are also present in the observations although not as evident as in the model (Figure 3a). Overall, the intensity, location, diurnal cycles of precipitation, the peak and minimum hours, and the phase delay along the Meiyu rainband are all reasonably well reproduced in the model forecasts. In the rest of this paper, model output will be used to perform diagnostic analyses, with the main goal of understanding the most important cause of the morning peak and afternoon-evening minimum in Meiyu precipitation.

3.3. Diurnal Variations of the South and North Bands of Precipitation

Figure 4 shows the composite (average) hourly precipitation of the south and north rainbands, at 08, 14, and 22 LST and 06 LST (of the second day). The composite represents a mean state of cases when the Meiyu rainband was in roughly the same latitudinal zone. Because there was a northward jump in the Meiyu location in the Meiyu period, leading to relatively large location differences in the two groups of rainbands, we produce the composites for the two groups separately. The two groups also have differences in their diurnal precipitation variations. The red parallelogram in the figure indicates the domain for later budget calculations.

At 08 LST (Figures 4a and 4e), the Meiyu rainband is best organized and strongest at the southern (Figure 4a) and northern (Figure 4e) locations. These bands are oriented west-southwest to east-northeast with a length of more than 1,300 km. In the early afternoon (Figures 4b and 4f), the rainband becomes broken and splits into somewhat disconnected patches in the western half of the domain while the band over eastern China remains continuous, consistent with the persistent afternoon precipitation seen in Figure 3d. At 14 LST, scattered afternoon thermal convection is evident over southern China near the coast, contributing to the afternoon secondary maximum seen in Figure 3c.

By 22 LST, however, the northern rainband has weakened markedly (Figure 4g), with the average hourly rain rates within most parts of the domain decreasing to below 0.2 mm, from above 3 mm in the morning. The southern band (Figure 4c) is also much weakened at the original location, while convective cells reminiscent of afternoon convection remain further south. Some of these cells might have resulted from southward propagation of the rainband cells. By 06 LST in the early morning of the next day, both rainbands have regained much of their strength (Figures 4d and 4h) although they are not as well organized yet, compared to those at 08 LST (Figures 4a and 4e).

The mean hourly rain rates within the parallelograms shown in Figure 4 for the two rainbands are plotted in Figure 5. It is clear that the north band has a pronounced minimum at around 23 LST and a maximum around 08 LST. The afternoon peak around 14 LST is hardly identifiable from the curve. For the south band, the evening minimum occurs around 00 LST, and the major morning peak also occurs at 08 LST. The

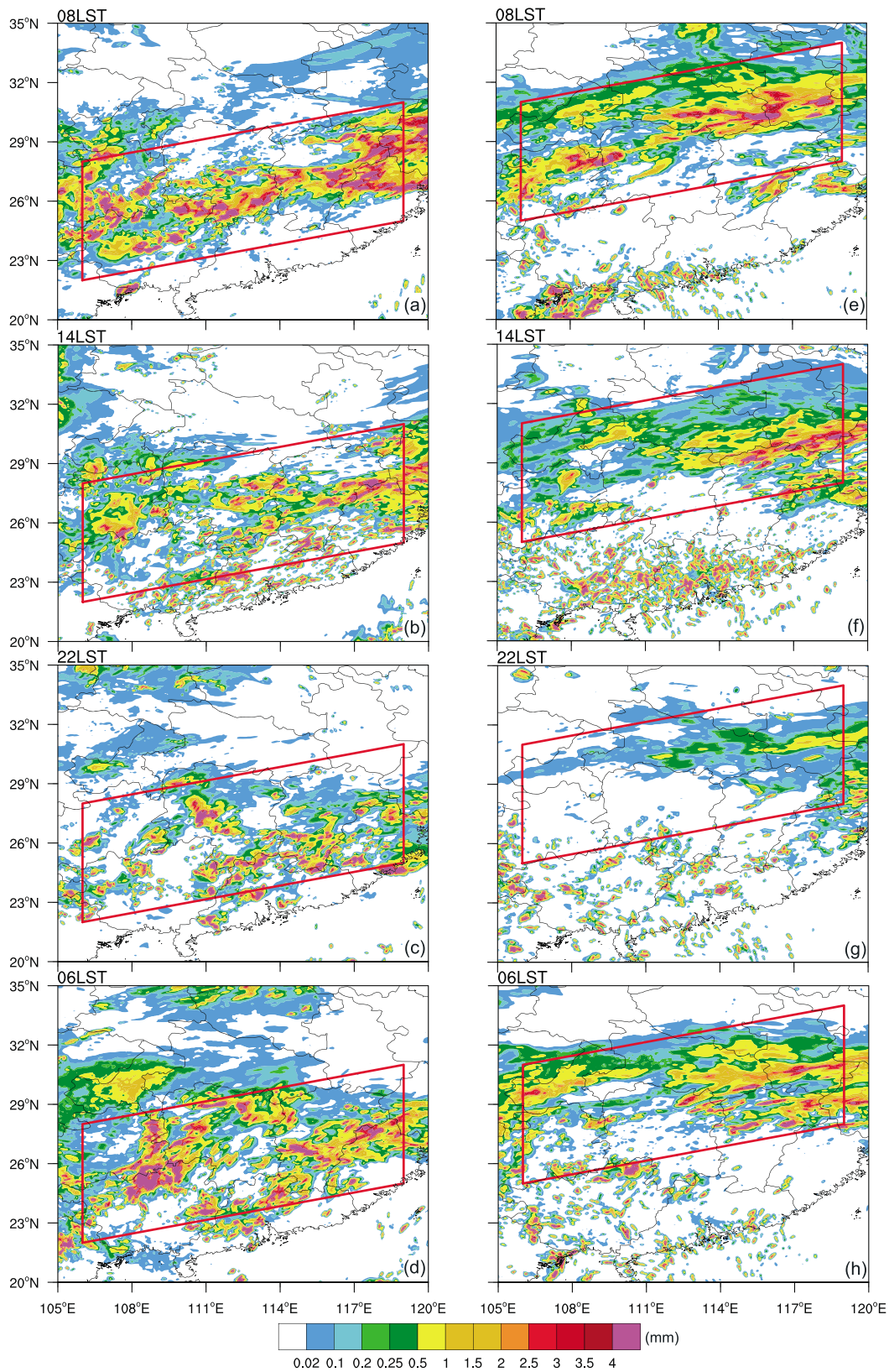


Figure 4. The composite (average) hourly accumulated Meiyu rainfall of the south rainband cases at (a) 08 LST (LST = UTC + 8 hr), (b) 14 LST, (c) 22 LST, and (d) 06 LST. (e)–(h) are the same as Figures 3a–3d but for the north rainband cases. Red parallelogram in left and right panels respectively denote the specific south and north rainband regions.

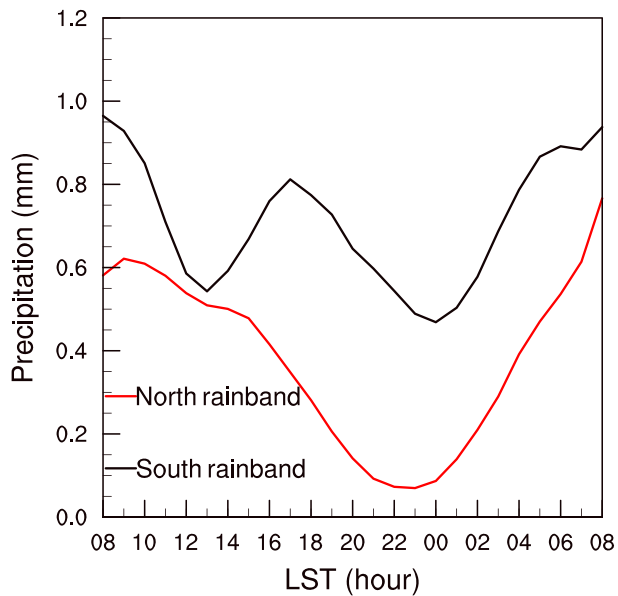


Figure 5. Diurnal variations of the mean hourly Meiyu precipitation rates over the south and north rainband regions.

secondary afternoon peak occurs at 17 LST, and it is much more pronounced than that of north band, reflecting more favorable conditions for afternoon thermal convection in the southern part of China. Compared the north band, the weakening of morning precipitation is faster with the south band after sunrise. Overall, the precipitation amount in the south band is much higher; even at the minimum, it is higher than that of north band most of the day. However, the overall amplitude of diurnal cycle is larger with the north band.

4. Boundary Layer Inertial Oscillations and Their Relationship With Meiyu Rainfall

4.1. Diurnal Variations of Low-Level Geostrophic and Ageostrophic Winds

Figure 6 presents the diurnal variations of composite large-scale fields that include the filtered geopotential height, the geostrophic, and ageostrophic winds at 925 hPa, the level where the nocturnal boundary layer LLJ is expected. The geostrophic wind vectors are clearly parallel to the geopotential height contours. The large-scale circulation patterns are maintained throughout the day, although there are some diurnal changes; there is a tendency for the western Pacific subtropical high (WPSH) to retreat toward the ocean in the afternoon and move back toward the interior continent at night. This should be due to daytime continental heating that reduces pressure over land more than over the ocean. We hypothesize that the effects of diurnal changes in large-scale circulation pattern on the Meiyu frontal precipitation is small compared to the effects of ageostrophic wind changes, to be examined below.

In comparison, there are very large diurnal changes with the ageostrophic wind vectors (Figure 6). For the south rainband, the southerly and southwesterly geostrophic flows between the WPSH and the low vortex over the Plateaus form a confluent Meiyu frontal zone with the low-pressure trough north of 29°N at 08 LST (Figure 6a). At this time, the ageostrophic wind speeds are as large as those of mean flow, and the winds are at large angles to the geopotential height contours and point toward the convergence zone from both south and north sides, creating significant low-level convergence forcing. The ageostrophic winds on the south side also significantly enhance the northward moisture fluxes into the frontal zone.

In the afternoon at 14 LST (Figure 6b), the geostrophic winds on the south side appear somewhat weakened with the slight retreat of WPSH. The ageostrophic winds become much weaker and are mostly parallel to the geostrophic winds on the south side, significantly reducing the convergence forcing in the frontal zone and the moisture transport into the zone. There are most synoptic-scale pattern changes at 20 LST as the WPSH retreats further and the trough to the north moves further east. Both geostrophic and ageostrophic winds along the southern boundary of the parallelogram are weak (Figure 6c), while ageostrophic winds across the northern boundary are much stronger. By 02 LST, much of the cross-isobaric ageostrophic winds seen at 08 LST has redeveloped near the southern boundary, contributing again significantly to the flow convergence within the frontal zone (Figure 6d). Over the next 6 hr, the WPSH moves inland further, accompanied by the associated northward flow advancement. At 08 LST, the wind directional shear is also the strongest in the frontal zone (Figure 6a). In general, there are clockwise rotations in the ageostrophic wind vectors throughout the day.

In the later period of the Meiyu season corresponding to most of the north band days, the WPSH advances further inland, and its diurnal position change, while still present, becomes less pronounced (right panels of Figure 6). This provides a more stable framework to apply the Blackadar inertial oscillation theory that assumes that the background pressure gradient field does not change. The north band cases are more representative of the typical YHRB Meiyu rainband (while the south band days are reminiscent of the late spring south China rainfall season).

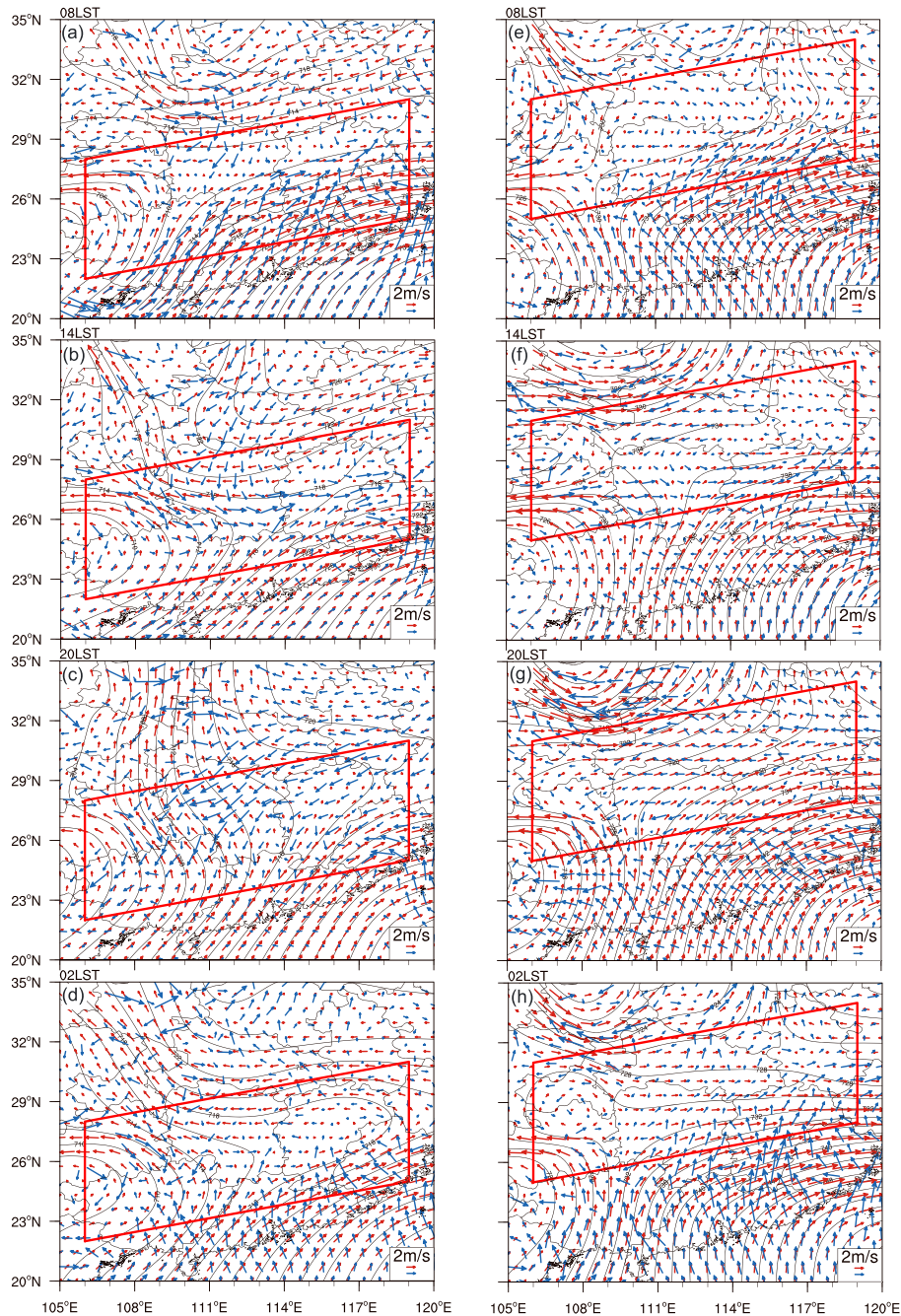


Figure 6. Composite, spatially filtered geopotential height (black lines), geostrophic winds (brown arrows), and ageostrophic winds (blue arrows) at 925 hPa of the south rainband days at (a) 08 LST, (b) 14 LST, (c) 20 LST, and (d) 02 LST. (e)–(h) are the same as Figures 6a–6d but for the north band days.

In the morning at 08 LST, perhaps partly due to the inland advancement of the WPSH, the higher-latitude low-pressure system is weak (Figure 6e). The seasonal advancement of summer monsoon concurrently with the northward advancement of WPSH creates a broad region of strong moisture transport from the southern oceans into the frontal zone. On the southern boundary of the parallelogram, the ageostrophic winds have significant cross-boundary components enhancing convergence forcing in the frontal zone (Figure 6e). By 14 LST, the ageostrophic winds have again rotated mostly into the geostrophic wind directions, removing much of the cross-boundary component. At 20 LST, the situation is still similar, except that the ageostrophic winds are now pointing northwestward on the south side. By 02 LST, a lot of the cross-isobaric ageostrophic

winds has redeveloped, contributing again to convergence into the frontal zone (Figure 6h). The above diurnal oscillations of low-level boundary layer flows, especially in the ageostrophic component, create diurnal variations in low-level convergence forcing and southerly moisture fluxes into the frontal zone that are consistent with the early morning precipitation peak and evening minimum observed with both south and north bands.

The diurnal changes in the ageostrophic winds cross the south boundary of the budget volumes (enclosed by the parallelograms) for the south and north bands are further examined by plotting them in vertical cross sections along the south boundaries (Figure 7). For the south band, in the morning at 08 LST, the ageostrophic winds below 700 hPa are almost unanimously directed toward the northeast and the maxima of over 4 m/s mainly exist below 850 hPa, along with the low-level southwesterly jet (Figure 7a). The north-south ageostrophic wind component has maximum values mainly between the 950 and 900 hPa levels where nocturnal LLJ is expected. By 14 LST, the ageostrophic winds are mostly directed toward the east but are much weaker (Figure 7b), and in the north-south direction the wind component turns negative (southward) at some locations at the low level (Figure 7b). Over the next 6 hr through evening, the ageostrophic winds remain weak and some northwesterly component develops near the western end (Figure 7c), and the northerly wind covers a larger area in the cross section, indicating further weakening of the low-level southwesterly flows. After midnight at 02 LST, strong southerly ageostrophic wind component redevelops below the 850 hPa level, with the wind vectors pointing mostly toward north-northwest (Figure 7d). The pattern of the north-south wind contour map of 02 LST is similar to that of 08 LST (Figure 7a) although the wind vectors have more of a westward component than an eastward component. The diurnal changes of the ageostrophic winds clearly indicate the development of boundary layer LLJ at night, and the ageostrophic wind vectors have clockwise rotation in direction, and the changes are consistent with what are observed from Figure 6.

For the north rainband, the overall diurnal variations of the ageostrophic winds across the southern boundary of its budget volume are similar to those of south band, but the magnitudes of variations are larger, with the southerly ageostrophic winds being stronger and deeper at night (Figures 7e and 7h). The northerly ageostrophic winds in the afternoon and evening are also stronger, but the maxima are close to the ground; the latter might have been enhanced by southward spreading outflow as the precipitation system tends to move southward when southerly monsoon flows weakens in the afternoon, as alluded to earlier in section 3.2.

4.2. Diurnal Variations of Moisture Fluxes Into Frontal Zone and Their Relationship With Meiyu Rainfall

In this subsection, we seek to more quantitatively evaluate the relationship between low-level moisture fluxes and Meiyu front rainfall. The moisture fluxes through the four boundaries of the parallelogram up to 700 hPa calculated according to $Q = -\frac{1}{g} \int_p^{p_{sfc}} Vqdp$ (V , q , g , p , and p_{sfc} are respectively the horizontal velocity vector, specific humidity, gravity acceleration, pressure and surface pressure), and sum of the four fluxes represent the net moisture convergence rate into the control volume enclosed by the parallelogram. The moisture fluxes below 700 hPa have been found to account for up to 80% of the column-integrated fluxes in earlier studies (G.-X. Chen et al., 2013, 2017).

Figure 8 shows that the moisture supplies for the south rainband (Figures 8a–8d) have two main sources, one from the Bay of Bengal and one from the South China Sea with the former being more dominant. On the northern boundary, the fluxes are inward most of the times also but much weaker than at the southern boundary. The main precipitation band is generally found near the northern edge of the southerly monsoon flows and is the strongest at 02 and 08 LST and weakest in the evening (Figure 8c). For the north rainband (Figures 8e–8h), with the WPSH advancing further inland, the moisture supplies come mainly from the South China Sea through the southern boundary of the control volume. The inward fluxes through the southern boundary are strongest at 08 and 02 LST (Figures 8e and 8h) and weakest at 20 LST (Figure 8g), and again the intensity of the rainband is in phase with the intensity of moisture fluxes through the southern boundary.

On average, the fluxes in the morning have magnitudes of more than $360 \text{ kg} \cdot \text{m}^{-1} \cdot \text{s}^{-1}$, and they reach minimum in the evening (e.g., Figures 8c and 8g) and strengthen again into the morning hours (Figures 8d and 8h). The variations in the moisture fluxes should be primarily due to the oscillations in wind speed and much less so due to variation in moisture content.

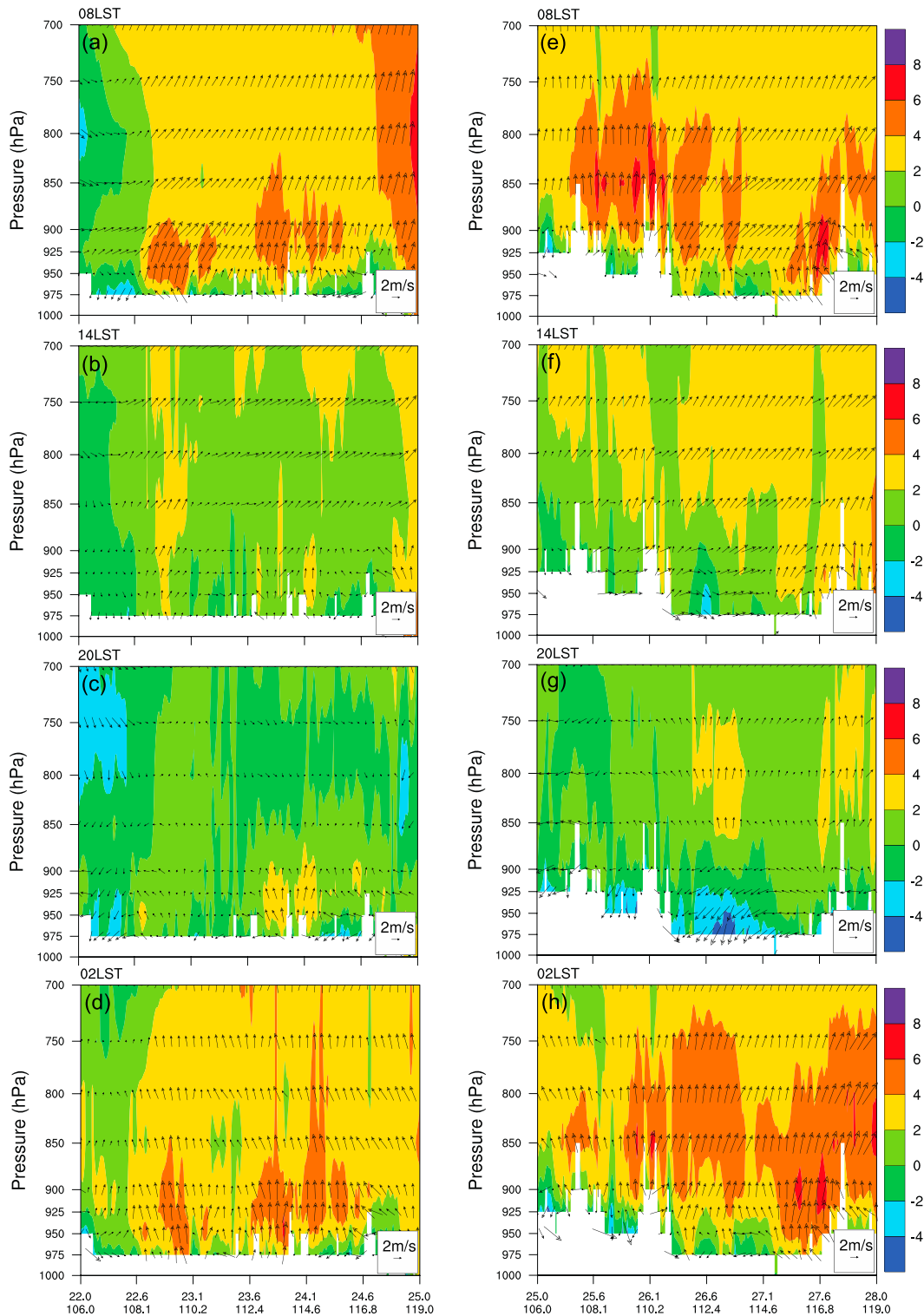


Figure 7. Composite ageostrophic south-north wind component (shaded) and horizontal ageostrophic wind vectors (with vector direction indicating compass directions) in the vertical plane along the south boundary of the budget volume of the south band at (a) 08 LST, (b) 14 LST, (c) 20 LST, and (d) 02 LST. In (e)–(h) are the corresponding fields for the north band.

The net moisture fluxes into the two control volumes due to total, geostrophic, and ageostrophic winds are plotted in Figure 9 as a function of the hour of day. The net fluxes due to geostrophic winds are very close to zero throughout the day for both bands, clearly because geostrophic winds are nearly nondivergent. So

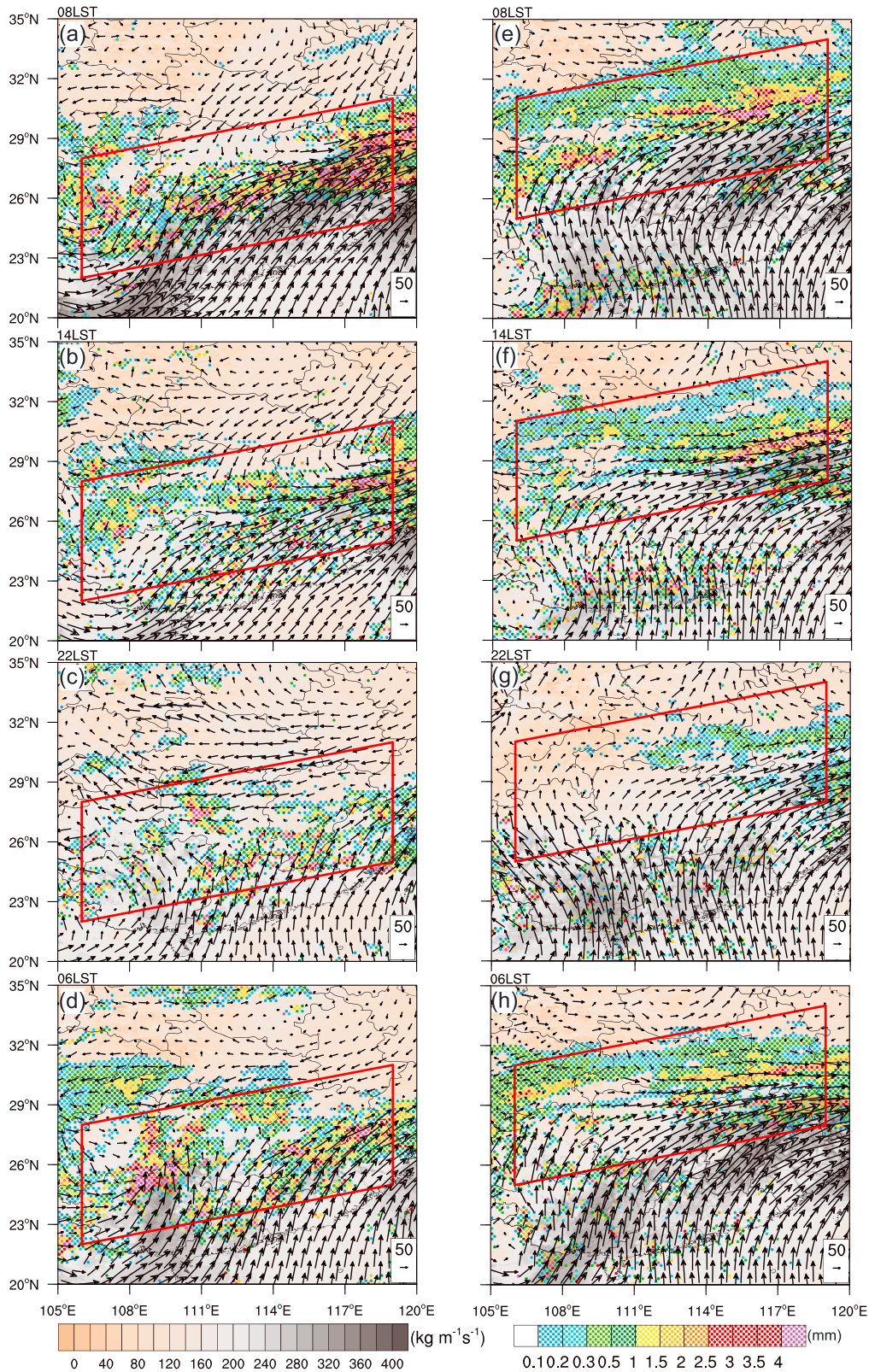


Figure 8. Composite moisture flux integrated in the lower troposphere ($1,000 \times 700$ hPa) (color shaded) and the precipitation rate (shading in colored dots) of the south rainband at (a) 08 LST, (b) 14 LST, (c) 20 LST, and (d) 06 LST. In (e)–(h) are the corresponding fields for north band. Arrows represent vector moisture fluxes. The vector key in the lower left corner is for $50 \text{ kg} \cdot \text{m}^{-2} \cdot \text{s}^{-1}$.

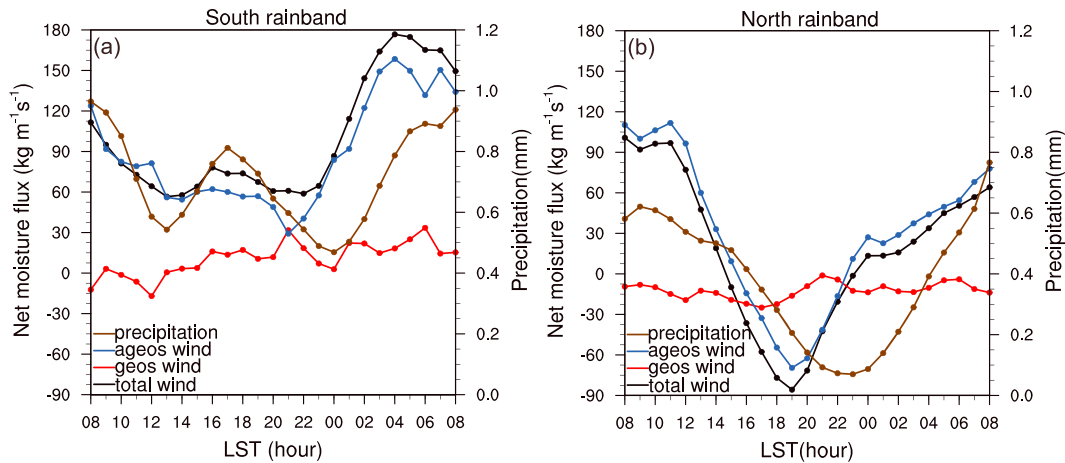


Figure 9. (a) Diurnal variations of net moisture fluxes into the budget region of the south rainband, due to the total wind (black line), geostrophic wind (red line) and ageostrophic wind (blue line) and the mean precipitation rate (green line) within the budget region. The fluxes are integrated from the surface to 700 hPa. (b) is the same as (a) but for the north band.

despite the confluent flows associated with the synoptic-scale pressure patterns into the frontal zone are strong (see Figure 6), they provide little low-level convergence forcing for triggering convection. The net ageostrophic moisture fluxes are much larger and are close to those of total winds (Figure 9). For the south band, the net flux had its maximum at 04 LST, the same as that of ageostrophic winds, and the maximum is 4 hr ahead of the precipitation peak hour of 08 LST (Figure 9a). The minimum net fluxes occur around 21 LST, about 3 hr ahead of the precipitation minimum, suggesting that the net flux peak is the cause rather than result of the precipitation peak. For the afternoon precipitation peaks around 17 LST, the total flux peak appears almost at the same time, consistent with the mutual support between the two peaks for deep thermal convection. Throughout the day, the net moisture flux remains positive (Figure 9a), supporting sustained, though diurnally varying rainfall throughout the day in the south rainband region.

For the northern band, a more pronounced net flux minimum is seen that precedes an equally pronounced precipitation minimum, by 3–4 hr again. In fact, after 14 LST, the net total wind flux turns negative, which means moisture is being drawn out of the control volume; as a result, existing precipitation rapidly decreases

until almost zero at 22 LST. After 19 LST, the net flux rapidly increases but it is not until 22 LST that the flux turns positive again; after that, total precipitation starts to increase again (Figure 9b), and reaching the maximum strength around 08 LST. The sequence of events shown by Figure 9 provides rather convincing evidences that the net moisture flux variations to a very large extent cause diurnal variations in precipitation in the Meiyu rainband, and the net moisture fluxes come almost exclusively from the ageostrophic wind component.

To more quantitatively assess the phase differences between the net flux and precipitation rate time series, we calculate time-lagged correlations between the two series for both bands (Figure 10). For the north band, the correlation is maximized with a 2- to 3-hr time lead in the net flux, while for the south band, the maximum occurs at a 2-hr lead time. This shorter lead time should be due to the contributions of mostly in-phase correlation between afternoon fluxes and precipitation (Figure 9a). At a phase lead of 2 to 3 hr, the correlation coefficient between the two time series is 0.77 and 0.86.

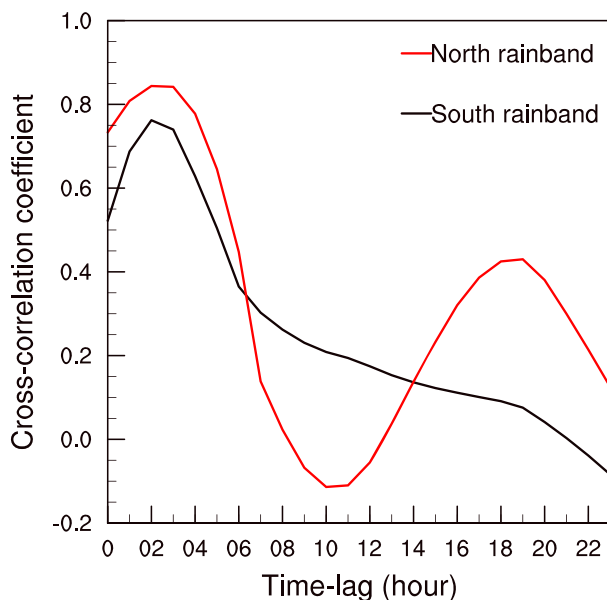


Figure 10. Lag correlation coefficients between the net moisture flux and the Meiyu precipitation within the south and north rainbands.

4.3. Ageostrophic Moisture Fluxes Into Frontal Zone and the Role of Boundary Layer Inertial Oscillations

Given that the geostrophic winds have little contribution to the net moisture flux into the low-level frontal zone, we focus on the

ageostrophic wind component in this subsection, including moisture fluxes of the ageostrophic winds, and their oscillation characteristics. In Figure 11, the clockwise rotational behaviors of the ageostrophic moisture fluxes (also ageostrophic wind itself, cf., Figure 6) are much more evident. For the two rainbands, at 08 LST, strong southwesterly ageostrophic flows transport extra moisture into the frontal zone through the southern boundary of the control volumes (Figures 11a and 11e). Some of the moisture fluxes exit the eastern boundary, while the fluxes through the northern boundary is weak. At 14 LST, most of the ageostrophic winds in the frontal regions turn clockwise toward the east, resulting much smaller net fluxes into the control volumes (Figures 11b and 11f). By 20 LST, the ageostrophic winds have turned about 160° toward west-southwest, again producing small net fluxes (Figures 11c and 11g). Between 14 and 20 LST, the fluxes at the west and south boundaries switch from being mostly inflow to mostly outflow and the reverse also happens to the east boundary (Figures 11c and 11g). In G.-X. Chen et al. (2013), such switching of moisture transport is also found at the west boundary of the Central China region and they attributed it to the mountain-plain solenoid as a part of reason; the mountain-plain solenoid should be taken into account but may not be the primary reason, since the switching is not limited to the western part of the domain that is close to high terrains. Over the next 6 hr, the ageostrophic winds turn further into mostly the northwest directions, normal to the southern boundary of the control volumes, resulting in large net moisture fluxes again (Figures 11d and 11h). Throughout the day, ageostrophic moisture fluxes through the southern boundary play the most critical rule.

Analogous to Figure 7, the vertical planes of composite ageostrophic moisture fluxes along the southern boundary are also presented in Figure 12. Overall, the diurnal variations of the ageostrophic moisture fluxes at the low levels are basically in line with the ageostrophic wind variations, also confirming that the flux changes in both the direction and value are essentially determined by the wind oscillations, and most of the variations occur the lower boundary layer. Specifically, at 08 LST, for the two rainbands, it is the southwesterly or southerly moisture inflows from the lower levels that contribute to the maximum moisture convergence into the frontal zone (Figures 12a and 12e). By 14 LST, in addition to the veering of the weakened ageostrophic moisture transport, some parts of the lower-level moisture inflows have turned into outflow, especially for the north rainband (Figures 12b and 12f), leading to the net moisture divergence in the following few hours (Figure 9b). At 20 LST, some of the lower-level outflows rotate toward southwest, especially for the north rainband (Figures 12c and 12g), corresponding to the maximum negative flux around this time (Figure 9b). At 02 LST, the low-level moisture inflows regain their strength.

Hourly variations of the mean vector moisture fluxes at each boundary are shown in Figure 13 to give a more direct view of flux direction changes. In the figure, the tips of the mean vector moisture fluxes are sequentially connected, and it can be seen that at all boundaries for both bands, both total and ageostrophic wind flux vectors show clockwise rotation, with the ageostrophic fluxes forming nearly closed circles while those of total fluxes tend to remain open due to diurnal changes in geostrophic winds. In about half of the cases, the ageostrophic circles enclose the coordinate origin (ageostrophic wind vector rotates around the origin as predicted by the Blackadar inertial oscillation theory) while in other cases the circles do not. The nonstationarity of the geostrophic flow around which the ageostrophic wind vector is supposed to rotate around should be part of the reason. Possible underestimation of the geostrophic component of the winds is another possible reason, given that the filter procedure used likely leads to underestimation of the horizontal pressure gradient. Still, the clockwise rotational behaviors indicate that the Blackadar's boundary layer inertial oscillation theory should explain to a large extent the systematic diurnal wind speed and direction changes seen here. With the theory, the amplitude of the ageostrophic wind is proportional to the speed of geostrophic wind; hence, the amplitudes of oscillations are the largest at the southern and western boundaries where the southerly and southwesterly monsoon flows are the strongest. This is consistent with the observation by G.-X. Chen et al. (2013) that diurnal variations of monsoon are stronger on days summer monsoon is active. On the northern boundary of the north band, the oscillation amplitude is the smallest (Figure 13h). The Blackadar theory also predicts strongest winds in the form of boundary layer LLJ around 3 LST, and the weakest winds in the afternoon when boundary layer mixing is the strongest.

We next look at flux contributions at individual boundaries, which are plotted in Figure 14. As mentioned, geostrophic winds and associated moisture fluxes exhibit small diurnal variations; we can see an increase in the geostrophic fluxes in the afternoon through evening, which can at least be partially attributed to the large-scale mountain-plains and land-ocean solenoids (during the day, stronger pressure gradient can

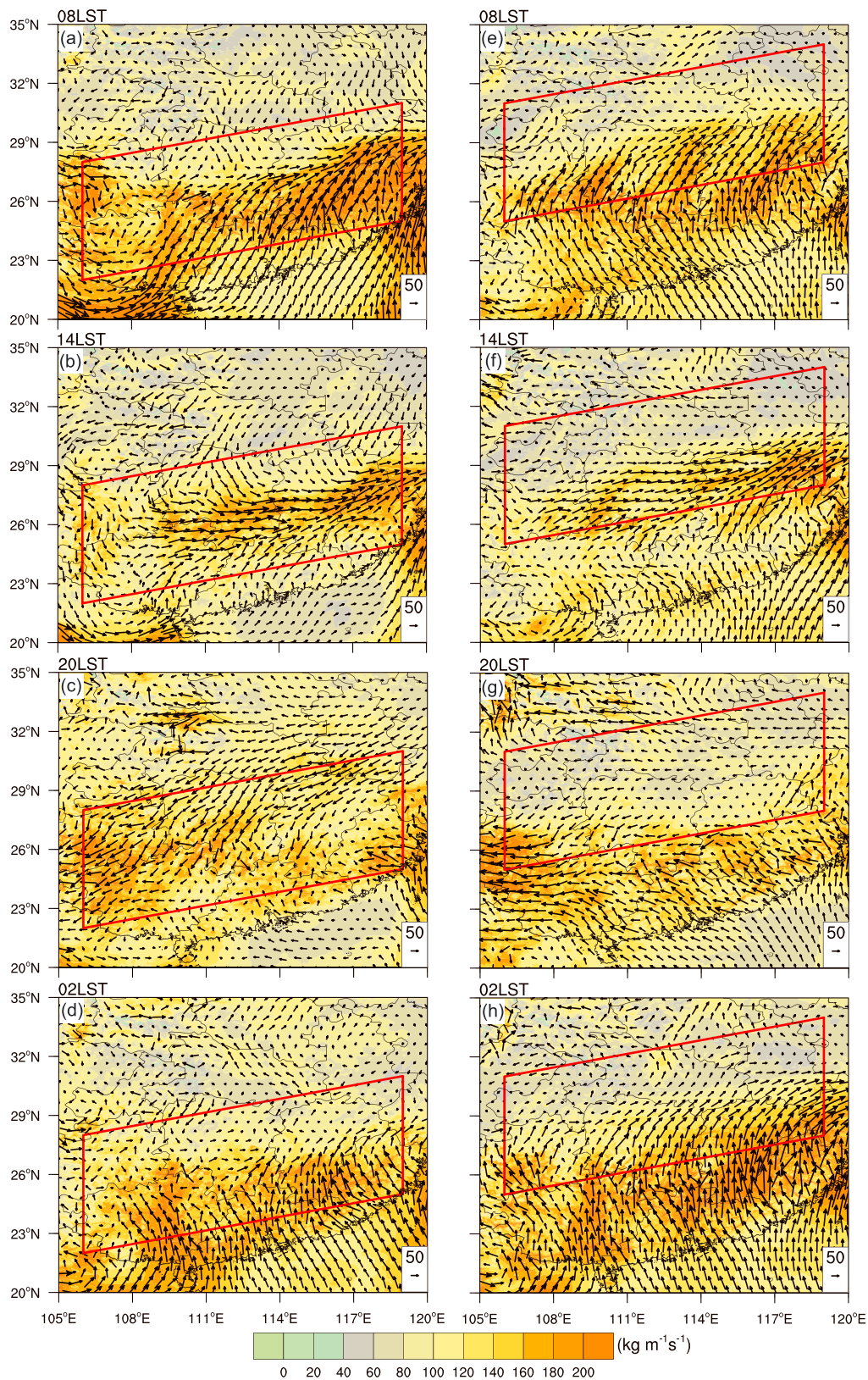


Figure 11. Composite ageostrophic moisture flux integrated in the lower troposphere (1,000–700 hPa; shaded) of the south rainband at (a) 08 LST, (b) 14 LST, (c) 22 LST, and (d) 02 LST. In (e)–(h) are the corresponding fields for the north rainband. Arrows represent the vector ageostrophic moisture fluxes.

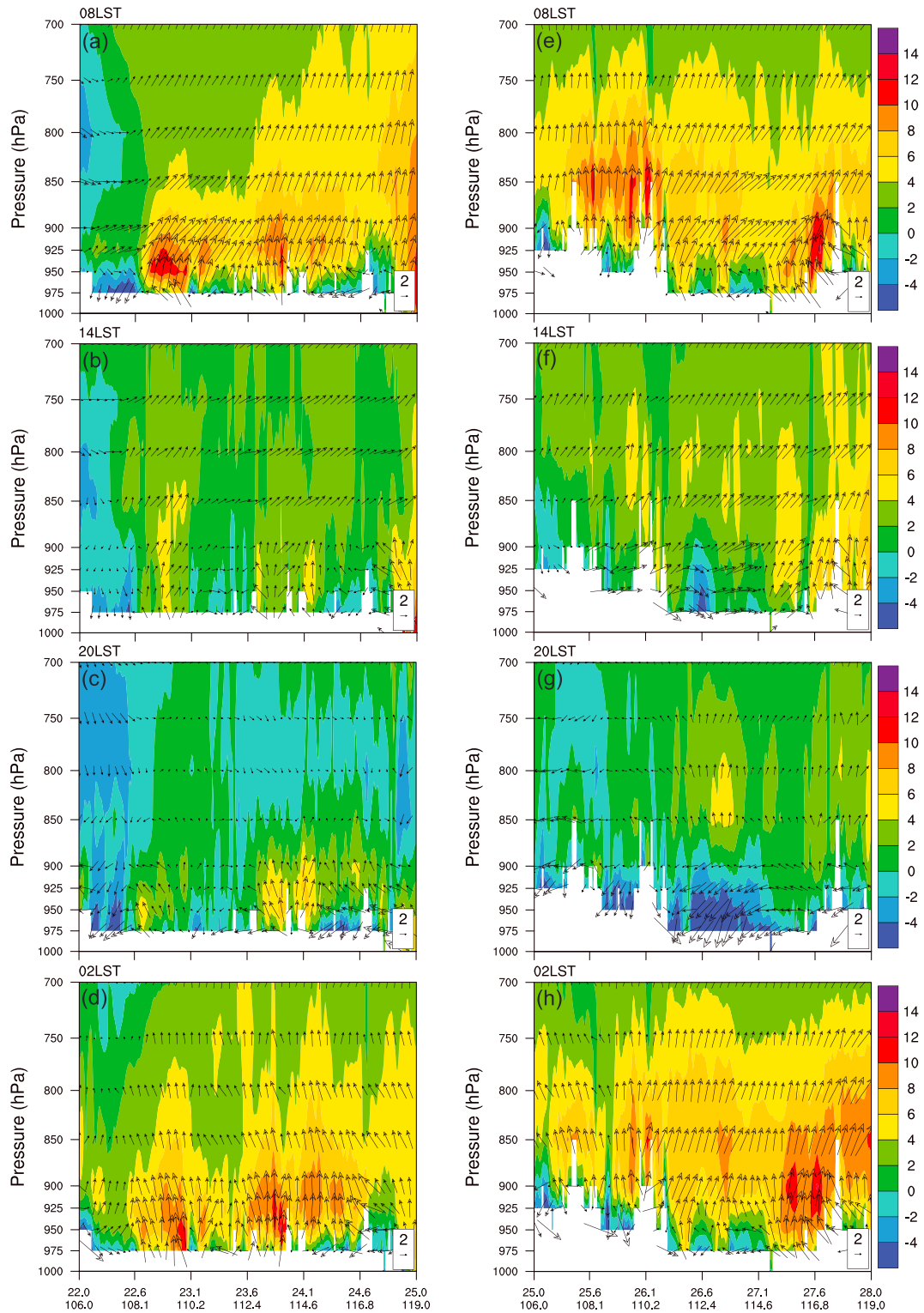


Figure 12. Composite ageostrophic moisture fluxes ($\text{kg} \cdot \text{m}^{-2} \cdot \text{s}^{-1}$) in the vertical plane along the south boundary of the control volume for south rainband (shaded) at (a) 08 LST, (b) 14 LST, (c) 20 LST, and (d) 02 LST. Arrows represent the vector horizontal ageostrophic moisture fluxes (with east-west and north-south components) in the cross section. In (e)–(h) are the corresponding plots for the north rainband.

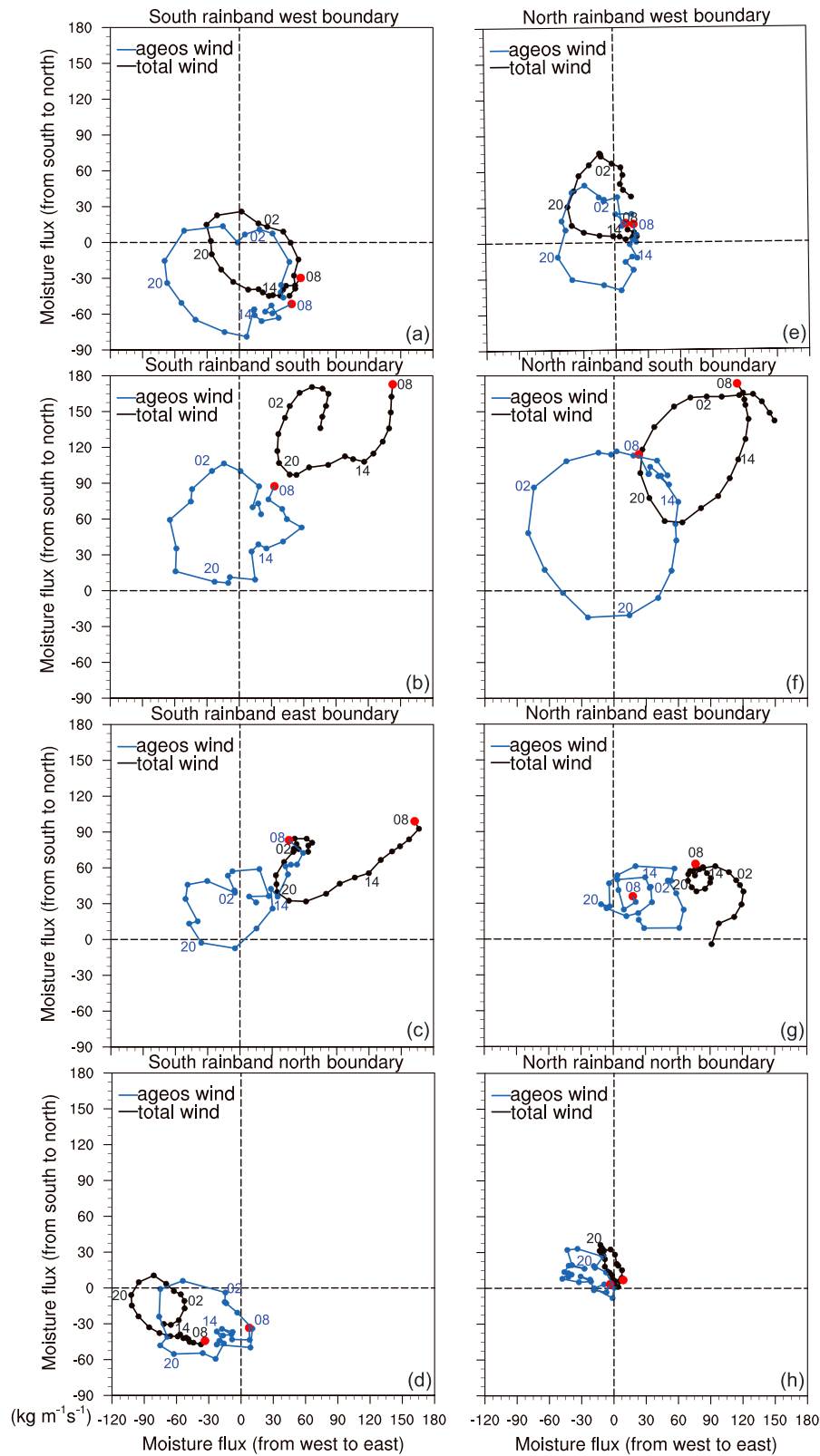


Figure 13. Plots of vector moisture fluxes by total wind (black line) and ageostrophic wind (blue line) through the (a) west, (b) south, (c) east, and (d) north boundaries of the south rainband control volume. (e)–(h) are the corresponding plots for the north rainband region. The dots on the curves correspond to the tips of the flux vectors and the red dot on each curve marks the start time at 08 LST.

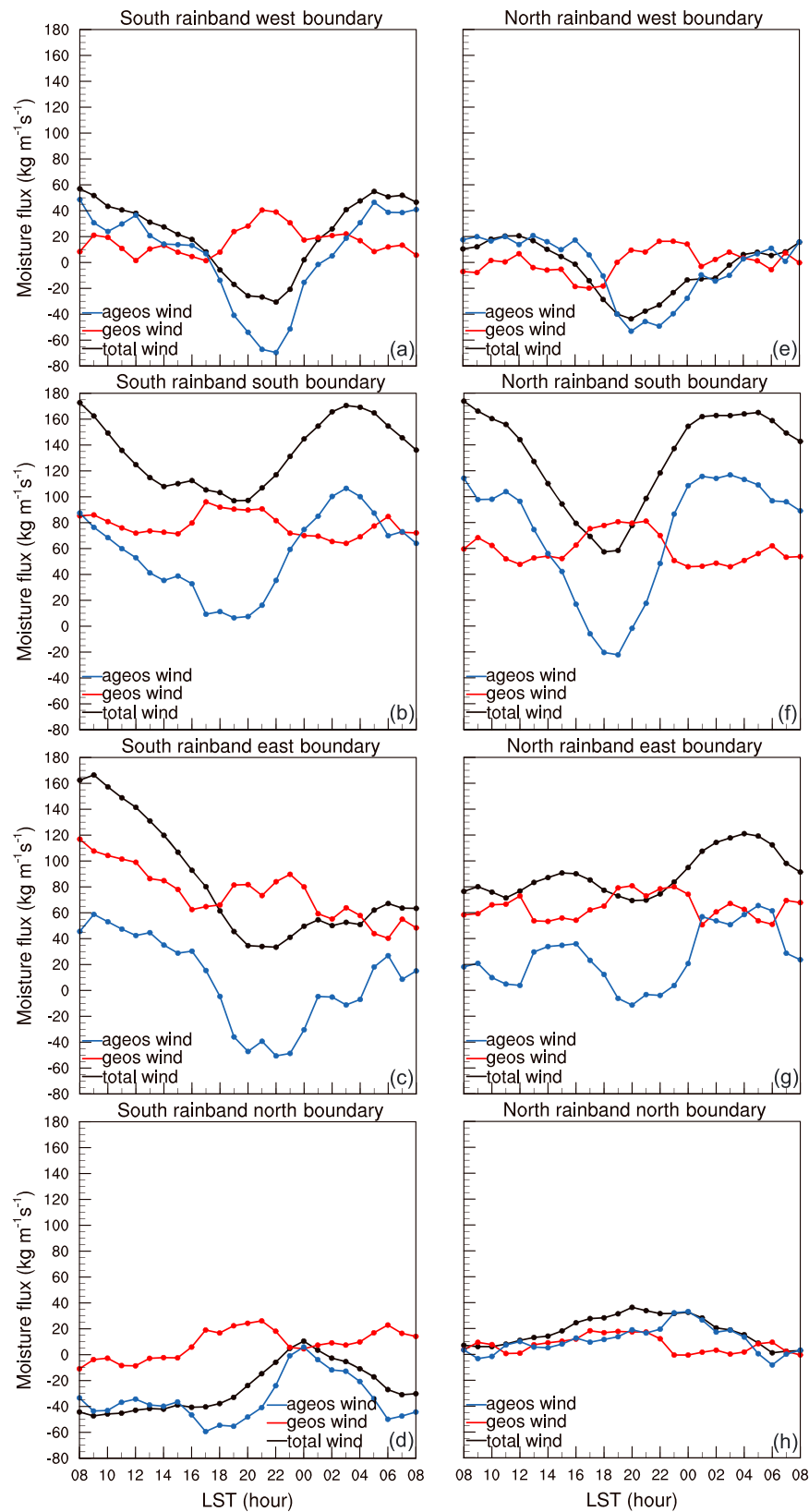


Figure 14. Diurnal variations of moisture fluxes by total winds (black line), geostrophic winds (red line), and ageostrophic winds (blue line) at (a) west, (b) south, (c) east, and (d) north boundary of the south rainband region. In (e)–(h) are the corresponding fluxes for the north rainband region.

develop between the WPSH and the lower pressure over the continent). The fluxes at the east and west boundaries tend to be in phase and those at the north and south boundaries also tend to be in phase; therefore, their contributions to the net fluxes tend to cancel each other, leading to small contributions to the net fluxes overall by the geostrophic fluxes.

At the east and west boundaries, the ageostrophic fluxes are also generally in phase, and the fluxes are generally positive from midnight through early afternoon, and negative in the evening, consistent with the fluxes seen in Figures 11 and 13. Such fluxes point mostly eastward at 14 LST and westward at 20 LST (Figure 11) and are consistent with the clockwise rotation due to inertial oscillations (Figure 13). At the west boundary, the diurnal variation of westerly inflow for the south band is more distinct, probably for being more affected by the mountain-plains circulations. At the northern boundary, the diurnal variations of fluxes of the north rainband are negligible (Figure 14h) result of weak geostrophic flows there (see also Figure 12h).

The relatively fast phase rotation for the north rainband seems to be more evident in Figure 14. For instance, at the south boundary, for the south rainband, the morning peak of southwesterly inflow occurs at 03 LST (Figure 14b) that is 2 hr later than the peak time for the north rainband (Figure 14f). The larger Coriolis parameter may have played a role (for faster rotation due to inertial oscillation), as may the geostrophic wind direction differences.

4.4. Relative Role of Latent Heat Feedback in Frontal Precipitation

Up till now, the fundamental role of boundary layer ageostrophic winds as caused by the inertial oscillations around the geostrophic winds in regulating the diurnal cycles of Meiyu frontal precipitation, both in creating early morning peak and evening minimum, has been reasonably well established. On the other hand, given the heavy and persistent precipitation involved, the latent heating can be a significant contributor to increasing and maintaining Meiyu frontogenesis and associated frontal circulations, thereby enhancing the lower tropospheric convergence and rainband development (Kuo & Anthes, 1982; Ding & Chan, 2005). For this reason, we ask the question: "What kind of role does the release of latent heating play in the Meiyu rainfall diurnal cycle and what is the consequence of the latent heat release?" We perform one specific experiment to help answer this question.

We choose the forecast starting from 12 UTC (20 LST) 29 June 2014 among the north rainband cases as a representative case and perform a sensitivity experiment that is the same as the original forecast except that latent heating is turned off 10 hr into the model simulation at 06 LST. In the experiment, condensation is still allowed to occur within the microphysics but the latent heat is discarded (this is the "fake dry" configuration of WRF). The experiment is called noLH and the original experiment is called CNTL. Other configurations of the WRF model are identical to those described in section 2.2. Figure 15 shows the hourly precipitation fields predicted by CNTL at 08, 14, 22, and 06 LST, which have pronounced diurnal variations. Specifically, an organized precipitation band is evident in the morning of 30 June (Figure 15a), and this rainband gradually weakens in the afternoon as the precipitation cores move eastward along the band (Figure 15b). The rainband is almost completely dissipated later into the evening with only some weak precipitation remaining (Figure 15c). By 06 LST of the next day, an intense rainband redeveloped that is almost continuous across three provinces from west to east, which is also better organized than that of previous morning (Figure 15a). Such diurnal variations in precipitation are typical of the Meiyu rainband cases sampled in this paper.

Specifically, the budget-domain-mean hourly rain rate in CNTL reaches a minimum at around 21 LST and peaks at around 07 LST of the second day morning (Figure 16a), which are in a general agreement with the diurnal variations of the north rainband composite shown in Figure 5. When latent heating is turned off in noLH (2 hr before the start of the plotted curve at 06 LST 30 June), the rainfall amount is greatly reduced, not surprisingly, and a minimum is also reached at around 21 LST (Figure 16a). After that time, the condensed liquid water and the surface-accumulated precipitation start to increase and reach peak values at around 06 LST (Figures 16a and 16b). Given the removal of latent heat release from the model within noLH, any condensed water is purely due to dynamic forcing, mostly associated the low-level flow convergence. All precipitation can be considered forced stable precipitation, and the maximum mean rainfall is about 30% that of the peak of CNTL, suggesting very significant roles played by the convergence forcing. The convergence forcing was strong enough to lift low-level air parcels to their lifted condensation levels, and the inclusion of latent heat release in CNTL does not change the overall phase of the precipitation diurnal cycles much,

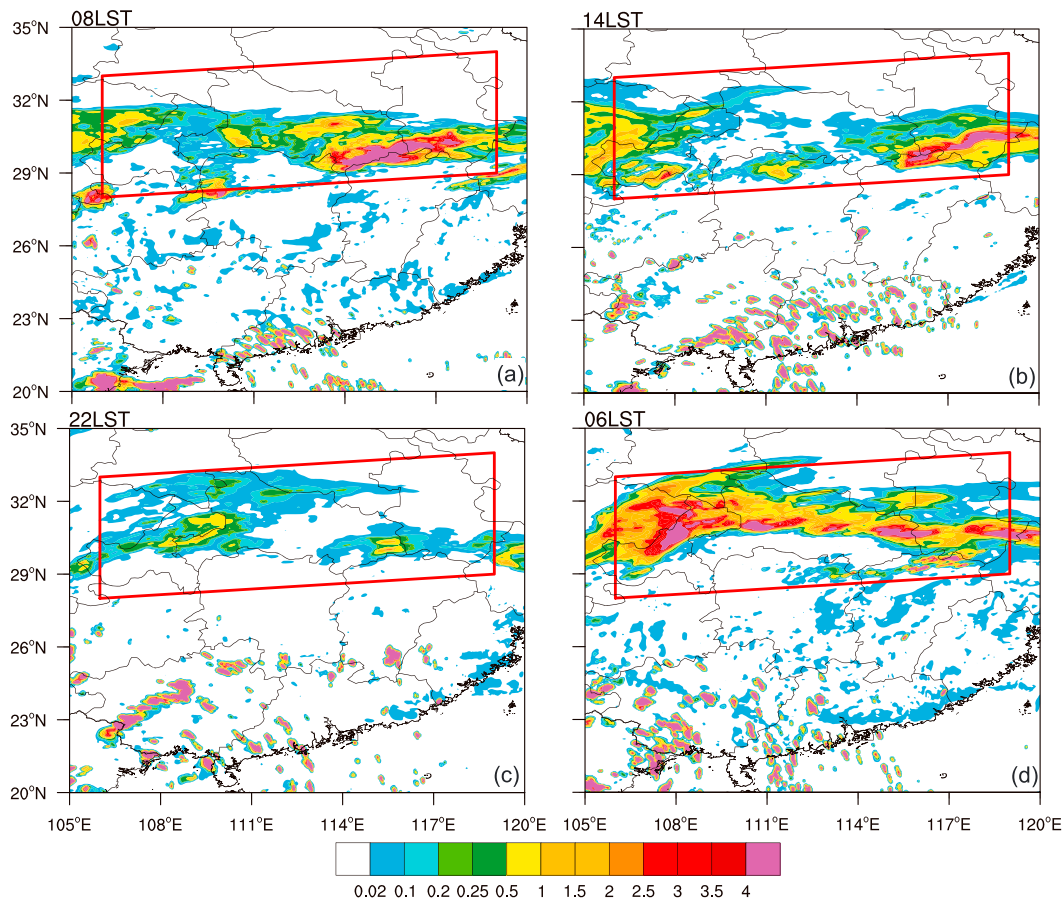


Figure 15. Predicted hourly accumulated precipitation (mm) in experiment CNTL of a Meiyu case from north rainband days at (a) 08, (b) 14, (c) 22, and (d) 06 LST. The model simulation started at 20 LST of 29 June 2014. The red parallelogram encloses the region for moisture flux budget analysis.

indicating that any positive feedback of the latent heat release associated with the enhanced nighttime precipitation play at most secondary role in modulating the precipitation diurnal cycles associated with the Meiyu rainband (although the latent heat does increase significantly the intensity of precipitation, as expected, and the latent heat causes the rain rate to continue to increase beyond the onset of enhanced convergence forcing after midnight). This is supported by the comparison of moisture fluxes through the four budget region boundaries. Figures 16c and 16d show that the differences between the moisture fluxes from CNTL and noLH are relatively small, especially for those at the southern boundary; the peak flux reached at 03 LST in noLH (Figure 16d) is no smaller than that in CNTL (Figure 16c). The largest difference exists between the fluxes through the eastern boundary, because the fluxes there are most affected by the convective scale circulations associated with the precipitation. The results from the no-latent-heat-release sensitivity experiment for a representative case presented in this section further confirm the dominant role of the inertial oscillations of southerly boundary layer monsoon flows in modulating the precipitation diurnal cycles of Meiyu precipitation over mainland China. Other effects including the latent heat release feedback are of secondary importance at most. We note here that larger differences may develop in the results if the simulation is run over several days; as cold pool from earlier precipitation can affect later convection; we interest here is on the immediate effect of latent heating within a single diurnal cycle though.

4.5. Conceptual Model

A conceptual model is proposed to summarize the key processes described above and is schematically illustrated in Figure 17. In the typical Meiyu season, strong southerly monsoon flows between the WPSH and a low-pressure system over the Yunnan-Guizhou and Tibet Plateaus to the west create a large-scale confluence

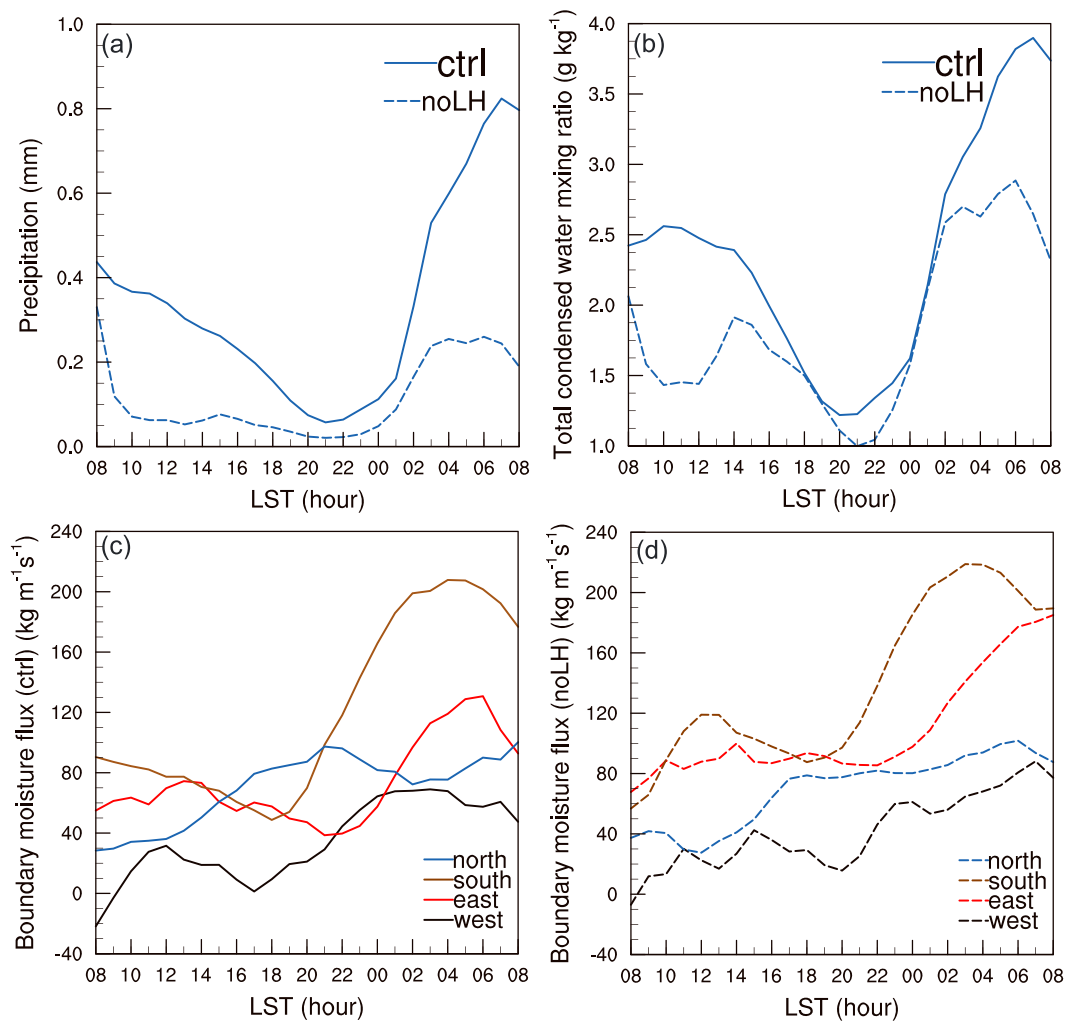


Figure 16. Diurnal variations of (a) simulated hourly precipitation and (b) total condensed water mixing ratio averaged in the budget region enclosed by the parallelogram in Figure 15 and up to 700 hPa, in experiments CNTL (solid line) and noLH (dashed line). Diurnal cycles of moisture fluxes through the four boundaries of the budget region are shown in (c) for CNTL and (d) for noLH.

zone with midlatitude flows from the north and a quasi-stationary Meiyu front between south China and YHRB regions. The geostrophic components of such flows are more or less nondivergent and hence do not contribute much to the low-level convergence forcing at the front. In another word, such flows form a roughly classic deformation field that is nondivergent (though it can be frontogenetic through the development of ageostrophic circulations but temperature gradient across Meiyu front is typically weak).

In the afternoon when active surface heating exists, surface friction and boundary layer mixing slow down the boundary layer flow significantly, making the total wind vector deviate to the left of the isobars and the geostrophic wind vector, creating a three-force-balanced state, and making the total wind speed subgeostrophic (see Figure 17b). After sunset in the evening, the boundary layer is stabilized and surface friction ceases to exert a drag on the boundary layer flow and the three-force balance in the afternoon is broken. The net force between the pressure gradient and Coriolis force then causes the flow to accelerate and according to the Blackadar inertial oscillation theory, the tip of ageostrophic wind vector will draw a full circle, clockwise, around the tip of the geostrophic wind vector, assuming that the background pressure gradient force does not change, and the surface friction of the next day does not interfere. The time to complete the full circle is $2\pi/f$, where f is the Coriolis parameter. This creates the inertial oscillations of the boundary layer flow. The magnitude of the ageostrophic wind is proportional to the background geostrophic wind so the stronger is the background (southerly monsoon) flow, the stronger is the ageostrophic inertial oscillation.

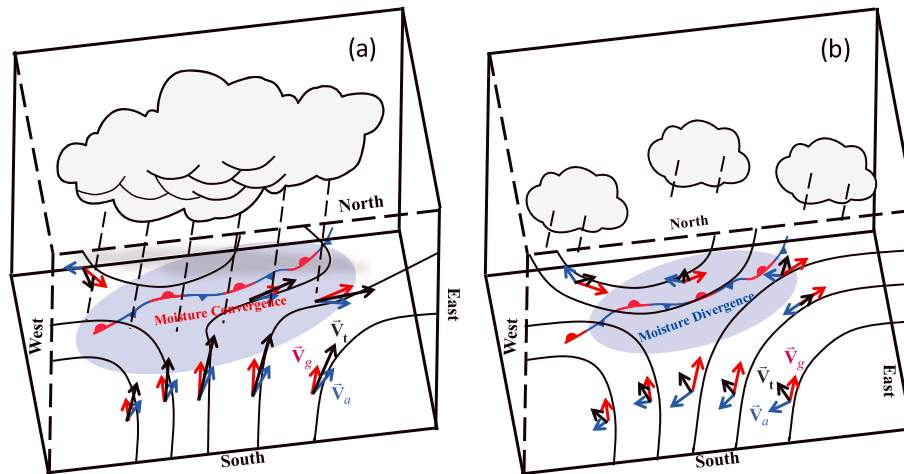


Figure 17. Conceptual diagram of diurnal variations of wind fields, including the total wind V_t (black arrows), geostrophic wind V_g (red arrows), and ageostrophic wind V_a (blue arrows) over the Meiyu rainband region in the (a) early morning and (b) late afternoon. The geopotential height contours also shown with black lines and the quasi-stationary Meiyu front is marked by standard symbols.

Usually between midnight and early morning, the ageostrophic wind vector points in a similar direction as the geostrophic wind, making the total wind supergeostrophic (see Figure 17a). It is the ageostrophic wind that creates low-level flow convergence and hence low-level lifting forcing. Strong, sustained supergeostrophic flows from the south also transport more moisture into the frontal zone. The two processes create precipitation maximum in the early morning, a few hours after the net moisture flux into the frontal zone reaches its maximum. In the afternoon, the ageostrophic winds are directed in roughly the opposite direction as the geostrophic winds, effectively drawing air out of the frontal zone, creating a net moisture flux out of the frontal zone, thereby causing the frontal precipitation to weaken quickly in the late afternoon and evening. As the southerly monsoon flows weaken in the afternoon, cold pool and gust front forming from morning precipitation in the Meiyu rainband region can push ahead toward the south, producing propagating squall lines that eventually detach itself from the main confluence zone and decay. Such behaviors are also suggested by Hovmöller diagrams of precipitation in observations and forecasts of 2013 and 2014 summer months (Zhu et al., 2018).

5. Summary and Conclusions

Convection-permitting 4-km WRF model forecasts together with dense rain gauge observations are used to investigate the primary cause for Meiyu precipitation diurnal cycles. During the Meiyu season in 2014, two main regions of Meiyu rainbands (respectively denoted as south and north rainbands) are found with pronounced diurnal variations. The general characteristics of precipitation are well captured in the WRF model. The south rainband has double rainfall peaks, in the afternoon and early morning, with the afternoon peak due to afternoon thermal heating. The north rainband exhibits only one peak in the morning.

The low-level ageostrophic winds exhibit evident diurnal clockwise rotations with significant regional differences. Given the diurnally varying winds, the net low-level moisture fluxes directed into the Meiyu frontal zone reach maximum a few hours after midnight, decrease by more than 50% in the afternoon and into night, and then quickly increase from midnight until reaching its peak again. The maximum and minimum of net moisture fluxes into the frontal zone are found to lead the corresponding extrema of precipitation by about 3 hr, while the correlation is the largest when the time series of hourly precipitation lags the net moisture flux time series by 2 to 3 hr.

Geostrophic winds are found to contribute very little to the net moisture fluxes hence very little to low-level convergence listing, while ageostrophic winds are responsible for most of the net moisture fluxes. The mean ageostrophic winds and associated moisture fluxes are shown to rotate clockwise to complete full circles within a day, rotating around the tips of geostrophic wind vectors. The clockwise rotations of ageostrophic winds within the boundary layer indicate that the Blackadar boundary layer inertial oscillation theory is at

work, and it can explain to a large extent the systematic diurnal wind speed and direction changes observed. According to the theory and consistent with the model results, the amplitudes of oscillations are generally proportional to the background geostrophic wind speed and that the maximum wind speed in the form of boundary layer LLJ occurs in early morning hours within the strong southerly monsoon flows directed into the Meiyu frontal zone. In the afternoon when the boundary layer LLJ is weakened most, the ageostrophic winds south of the Meiyu rainband act to “suck” air out of the frontal zone and significantly weaken the precipitation, creating an afternoon minimum.

In a sensitivity experiment that removes the released latent heat from the simulation, the phase of precipitation diurnal cycles remains unchanged indicating at most secondary role of the precipitation feedback in modulating the precipitation diurnal cycles. Solenoidal circulations between the Tibet Plateau and the central and eastern China Plains, as suggested by previous authors, also likely play only secondary roles.

A conceptual model summarizing the processes is proposed. Our results also suggest that the treatment of boundary layer processes, including PBL parameterizations, is important for accurate prediction of Meiyu frontal precipitation, as is the proper measurement and initialization through advanced data assimilation of ageostrophic flows in the Meiyu frontal system. The latter is usually not handled well by large-scale data assimilation systems.

Finally, point out that the connection between diurnal variation of precipitation over southeastern China in the active summer monsoon season and the so-called DMV had been quite well recognized rather by previous studies (G.-X. Chen et al., 2009a, 2009b), but the cause of the DMV was not well understood. However, essentially all characteristics of the DMV, as described in G.-X. Chen et al. (2009b), match those of the boundary layer inertial oscillations predicted by the Blackadar’s theory, and such oscillations are the strongest when the prevailing geostrophic winds, that is, the southwesterly monsoon flows, are strong and persistent. Therefore, this paper also serves to point out that the DMV identified in previous studies is actually primarily caused by the boundary layer inertial oscillations as the southerly monsoon flows experience deceleration during the day due to surface friction, and supergeostrophic acceleration at night when the boundary layer flow decouples the ground surface, and the deviation winds rotate clockwise in direction.

Appendix A: Low-Pass Barnes Filter Used to Smooth Geopotential Height Fields

As stated in section 2.3, we obtain the geostrophic winds from the geopotential height field that is first smoothed by applying a low-pass Barnes filter. The Barnes filter was designed as part of an objective analysis scheme (Barnes, 1964). An example of using the filter to separate flows fields into large, mesoscale and convective scale can be found in X. Xu et al. (2017). The objective analysis scheme obtains a gridded field $A(x, y)$ from N values A_k ($k = 1, 2, \dots, N$) distributed in space at regular or irregular grid points based on successive corrections (in our case A_k is the original WRF model output or the unfiltered values). A first guess value, A_0 , at grid point (i, j) , is first obtained from the following equation,

$$A_0(i, j) = \sum_{k=1}^N w_k A_k / \sum_{k=1}^N w_k, \quad (A1)$$

where $w_k = \exp(-R_k^2/4c)$ is the weight function and R_k is the distance between grid point (i, j) and A_k . c is a specified constant.

Second, one correction is made to the first-guess field according to

$$A(i, j) = A_0(i, j) + \sum_{k=1}^N w'_k E_k / \sum_{k=1}^N w'_k \quad (A2)$$

wherein $E_k = A_k - A_{0k}$ is the difference between the original value and the first-guess field at the A_k location and the modified weight function w'_k is computed as $w'_k = \exp(-R_k^2/4cg)$ for $0 < g < 1$. Apparently, the scales retained in the filtered field depend on the choices of constants c and g . The final response as a function of wavelength λ is given by

$$R(\lambda) = R_0 \left(1 + R_0^{g-1} - R_0^g \right), \quad (A3)$$

where $R_0(\lambda) = \exp(-\pi^2 4c/\lambda^2)$ is the response function of formula (A1). The response function $R(\lambda)$ represents

the percentage of one particular wave amplitude that remains after applying the “filtering” or “objective analysis” procedure.

Acknowledgments

This work was primarily supported by the Natural Science Foundation of China grants 41730965 and 41230421, and The National Key Basic Research “973” Program of China (2013CB430103). Xia Luo gratefully acknowledges financial support from the China Scholarship Council that enabled her extended visit to the University of Oklahoma. We thank the anonymous reviewers for their comments that improved this article. The data, including rain gauge observations and WRF forecasts, are available at <https://pan.baidu.com/s/114MiHqXcrlWZYrronxhaFw> (password: key6). For more detailed data, please contact us via e-mail.

References

- Bao, X., & Zhang, F. (2013). Impacts of the mountain–plains solenoid and cold pool dynamics on the diurnal variation of warm-season precipitation over northern China. *Atmospheric Chemistry and Physics*, *13*, 6965–6982.
- Bao, X., Zhang, F., & Sun, J. (2011). Diurnal variations of warm-season precipitation east of the Tibetan Plateau over China. *Monthly Weather Review*, *139*(9), 2790–2810. <https://doi.org/10.1175/MWR-D-11-00006.1>
- Barnes, S. L. (1964). A technique for maximizing details in numerical weather map analysis. *Journal of Applied Meteorology*, *3*(4), 396–409. [https://doi.org/10.1175/1520-0450\(1964\)003<0396:ATFMDI>2.0.CO;2](https://doi.org/10.1175/1520-0450(1964)003<0396:ATFMDI>2.0.CO;2)
- Blackadar, A. K. (1957). Boundary layer wind maxima and their significance for the growth of nocturnal inversions. *Bulletin of the American Meteorological Society*, *38*, 283–290.
- Bonner, W. D. (1966). Case study of thunderstorm activity in relation to the low-level jet. *Monthly Weather Review*, *94*(3), 167–178. [https://doi.org/10.1175/1520-0493\(1966\)094<0167:CSOTA1>2.3.CO;2](https://doi.org/10.1175/1520-0493(1966)094<0167:CSOTA1>2.3.CO;2)
- Carbone, R. E., & Tuttle, J. D. (2008). Rainfall occurrence in the United States warm season: The diurnal cycle. *Journal of Climate*, *21*(16), 4132–4146. <https://doi.org/10.1175/2008JCLI2275.1>
- Chang, C. P., Zhang, Y., & Li, T. (2000). Interannual and interdecadal variations of the East Asian summer monsoon and tropical Pacific SSTs. Part I: Roles of the subtropical ridge. *Journal of Climate*, *13*(24), 4310–4325. [https://doi.org/10.1175/1520-0442\(2000\)013<4310:IAIVOT>2.0.CO;2](https://doi.org/10.1175/1520-0442(2000)013<4310:IAIVOT>2.0.CO;2)
- Chen, G. T.-J., Wang, C.-C., & Lin, D. T.-W. (2005). Characteristics of low-level jets over northern Taiwan in Meiyu Season and their relationship to heavy rain events. *Monthly Weather Review*, *133*(1), 20–43. <https://doi.org/10.1175/MWR-2813.1>
- Chen, G. T.-J., & Yu, C. C. (1988). Study of low-level jet and extremely heavy rainfall over northern Taiwan in the Meiyu season. *Monthly Weather Review*, *116*(4), 884–891. [https://doi.org/10.1175/1520-0493\(1988\)116<0884:SOLLJA>2.0.CO;2](https://doi.org/10.1175/1520-0493(1988)116<0884:SOLLJA>2.0.CO;2)
- Chen, G.-X., Sha, W., & Iwasaki, T. (2009a). Diurnal variation of precipitation over southeastern China: Spatial distribution and its seasonality. *Journal of Geophysical Research*, *114*, D13103. <https://doi.org/10.1029/2008JD011103>
- Chen, G.-X., Sha, W., & Iwasaki, T. (2009b). Diurnal variation of precipitation over southeastern China: 2. Impact of the diurnal monsoon variability. *Journal of Geophysical Research*, *114*, D21105. <https://doi.org/10.1029/2009JD012181>
- Chen, G.-X., Sha, W., Iwasaki, T., & Ueno, K. (2012). Diurnal variation of rainfall in the Yangtze River Valley during the spring–summer transition from TRMM measurements. *Journal of Geophysical Research*, *117*, D06106. <https://doi.org/10.1029/2011JD017056>
- Chen, G.-X., Sha, W., Iwasaki, T., & Wen, Z. (2017). Diurnal cycle of a heavy rainfall corridor over East Asia. *Monthly Weather Review*, *45*, 3365–3389.
- Chen, G.-X., Sha, W., Sawada, M., & Iwasaki, T. (2013). Influence of summer monsoon diurnal cycle on moisture transport and precipitation over eastern China. *Journal of Geophysical Research*, *118*, 3163–3177. <https://doi.org/10.1002/jgrd.50337>
- Chen, H., Yu, R., Li, J., Yuan, W., & Zhou, T. (2010). Why nocturnal long-duration rainfall presents an eastward-delayed diurnal phase of rainfall down the Yangtze River Valley. *Journal of Climate*, *23*(4), 905–917. <https://doi.org/10.1175/2009JCLI3187.1>
- Chen, X.-C., Zhao, K., & Xue, M. (2014). Spatial and temporal characteristics of warm season convection over Pearl River Delta region, China, based on 3 years of operational radar data. *Journal of Geophysical Research: Atmospheres*, *119*, 12,447–12,465. <https://doi.org/10.1002/2014JD021965>
- Chen, X.-C., Zhao, K., Xue, M., Zhou, B., & Xu, W. (2015). Radar-observed diurnal cycle and propagation of convection over the Pearl River Delta during Mei-Yu season. *Journal of Geophysical Research: Atmospheres*, *120*, 12,557–12,575. <https://doi.org/10.1002/2015JD023872>
- Ding, Y. (1992). Summer monsoon rainfalls in China. *Journal of the Meteorological Society of Japan*, *70*(1B), 373–396. https://doi.org/10.2151/jmsj1965.70.1B_373
- Ding, Y., & Chan, J. C. L. (2005). The East Asian summer monsoon: An overview. *Meteorology and Atmospheric Physics*, *89*(1–4), 117–142. <https://doi.org/10.1007/s00703-005-0125-z>
- Ding, Y., Zhang, Y., Ma, Q., & Hu, G. (2001). Analysis of the large-scale circulation features and synoptic systems in East Asia during the intensive observation period of GAME/HUBEX. *Journal of the Meteorological Society of Japan*, *79*, 277–300.
- Du, Y., Chen, Y.-L., & Zhang, Q. (2015). Numerical simulations of the boundary layer jet off the southeastern coast of China. *Monthly Weather Review*, *143*(4), 1212–1231. <https://doi.org/10.1175/mwr-d-14-00348.1>
- Du, Y., Rotunno, R., & Zhang, Q. (2015). Analysis of WRF-simulated diurnal boundary layer winds in eastern China using a simple 1D model. *Journal of the Atmospheric Sciences*, *72*(2), 714–727. <https://doi.org/10.1175/jas-d-14-0186.1>
- Du, Y., & Zhang, Q. (2012). Characteristics of low-level jets in Shanghai during the 2008 and 2009 warm seasons as inferred from wind profiler radar data. *Journal of the Meteorological Society of Japan*, *90*(6), 891–903. <https://doi.org/10.2151/jmsj.2012-603>
- Du, Y., Zhang, Q., Chen, Y.-L., Zhao, Y., & Wang, X. (2014). Numerical simulations of spatial distributions and diurnal variations of low-level jets in China during early summer. *Journal of Climate*, *27*(15), 5747–5767. <https://doi.org/10.1175/JCLI-D-13-00571.1>
- Geng, B., & Yamada, H. (2007). Diurnal variations of the Meiyu/Baiu rain belt. *SOLA*, *3*, 61–64. <https://doi.org/10.2151/sola.2007-016>
- He, H., & Zhang, F. (2010). Diurnal variations of warm-season precipitation over northern China. *Monthly Weather Review*, *138*(4), 1017–1025. <https://doi.org/10.1175/2010MWR3356.1>
- Helfand, H. M., & Schubert, S. D. (1995). Climatology of the simulated Great Plains low-level jet and its contribution to the continental moisture budget of the United States. *Journal of Climate*, *8*(4), 784–806. [https://doi.org/10.1175/1520-0442\(1995\)008<0784:COTSGP>2.0.CO;2](https://doi.org/10.1175/1520-0442(1995)008<0784:COTSGP>2.0.CO;2)
- Hirose, M., & Nakamura, K. (2005). Spatial and diurnal variation of precipitation systems over Asia observed by the TRMM Precipitation Radar. *Journal of Geophysical Research*, *110*, D05106. <https://doi.org/10.1029/2004JD004815>
- Holton, J. R. (1967). The diurnal boundary layer wind oscillation above sloping terrain. *Tellus*, *19*(2), 199–205. <https://doi.org/10.1111/j.2153-3490.1967.tb01473.x>
- Huang, H., Wang, C., Chen, G. T., & Carbone, R. E. (2010). The role of diurnal solenoidal circulation on propagating rainfall episodes near the eastern Tibetan Plateau. *Monthly Weather Review*, *138*(7), 2975–2989. <https://doi.org/10.1175/2010MWR3225.1>
- Klein, P. M., Hu, X.-M., Shapiro, A., & Xue, M. (2016). Linkages between boundary-layer structure and the development of nocturnal low-level jets in Central Oklahoma. *Boundary-Layer Meteorology*, *158*(3), 383–408. <https://doi.org/10.1007/s10546-015-0097-6>
- Koch, S. E., DesJardins, M., & Kocin, P. J. (1983). An interactive Barnes objective map analysis scheme for use with satellite and conventional data. *Journal of Climate and Applied Meteorology*, *22*(9), 1487–1503. [https://doi.org/10.1175/1520-0450\(1983\)022<1487:AIBOMA>2.0.CO;2](https://doi.org/10.1175/1520-0450(1983)022<1487:AIBOMA>2.0.CO;2)

- Kuo, Y. H., & Anthes, R. A. (1982). Numerical simulation of a Meiyu system over southeastern Asia. *Paper Meteorological Research*, 5, 15–36.
- Li, J., & Chen, Y.-L. (1998). Barrier jets during TAMEX. *Monthly Weather Review*, 126(4), 959–971. [https://doi.org/10.1175/1520-0493\(1998\)126<0959:BJDT>2.0.CO;2](https://doi.org/10.1175/1520-0493(1998)126<0959:BJDT>2.0.CO;2)
- Li, T., Wang, B., Wu, B., Zhou, T., Chang, C.-P., & Zhang, R. (2017). Theories on formation of an anomalous anticyclone in western North Pacific during El Niño: A review. *Journal of Meteorological Research*, 31(6), 987–1006. <https://doi.org/10.1007/s13351-017-7147-6>
- Luo, Y., Qian, W., Zhang, R., & Zhang, D.-L. (2013). Gridded hourly precipitation analysis from high-density rain-gauge network over the Yangtze-Huai Rivers basin during the 2007 Meiyu season and comparison with CMORPH. *Journal of Hydrometeorology*, 14(4), 1243–1258. <https://doi.org/10.1175/JHM-D-12-0133.1>
- Markowski, P. M., & Richardson, Y. (2010). *Mesoscale meteorology in midlatitudes* (424 pp.). Chichester, UK: Wiley-Blackwell. <https://doi.org/10.1002/9780470682104>
- Morrison, H., Thompson, G., & Tatarskii, V. (2009). Impact of cloud microphysics on the development of trailing stratiform precipitation in a simulated squall line: Comparison of one- and two-moment schemes. *Monthly Weather Review*, 137(3), 991–1007. <https://doi.org/10.1175/2008mwr2556.1>
- Pan, Y., Shen, Y., Yu, Q.-Q., & Zhao, P. (2012). Merged analyses of gauge-satellite hourly precipitation over China based on OI technique (in Chinese with English abstract). *Acta Meteorologica Sinica*, 70, 1381–1389.
- Pleim, J. E. (2007). A combined local and nonlocal closure model for the atmospheric boundary layer. Part I: Model description and testing. *Journal of Applied Meteorology and Climatology*, 46, 1383–1395.
- Pleim, J. E., & Xiu, A. (1995). Development and testing of a surface flux and planetary boundary layer model for application in mesoscale models. *Journal of Applied Meteorological Sciences*, 34(1), 16–32. <https://doi.org/10.1175/1520-0450-34.1.16>
- Powers, J. G., Klemp, J. B., Skamarock, W. C., Davis, C. A., Dudhia, J., Gill, D. O., et al. (2017). The weather research and forecasting model: Overview, system efforts, and future directions. *Bulletin of the American Meteorological Society*, 98(8), 1717–1737. <https://doi.org/10.1175/BAMS-D-15-00308.1>
- Sampe, T., & Xie, S. (2010). Large-scale dynamics of the Meiyu-Baiu Rainband: Environmental forcing by the westerly jet. *Journal of Climate*, 23(1), 113–134. <https://doi.org/10.1175/2009JCLI3128.1>
- Shapiro, A., Fedorovich, E., & Rahimi, S. (2016). A unified theory for the Great Plains nocturnal low-level jet. *Journal of the Atmospheric Sciences*, 73(8), 3037–3057. <https://doi.org/10.1175/JAS-D-15-0307.1>
- Skamarock, W. C., Klemp, J. B., Dudhia, J., Gill, D. O., Barker, D. M., Wang, W., & Powers, J. D. (2005). A description of the Advanced Research WRF Version 2. 88 pp.
- Sun, J., & Zhang, F. (2012). Impacts of mountain–plains solenoid on diurnal variations of rainfalls along the Mei-Yu Front over the East China Plains. *Monthly Weather Review*, 140(2), 379–397. <https://doi.org/10.1175/MWR-D-11-00041.1>
- Trier, S. B., Davis, C. A., & Carbone, R. E. (2014). Mechanisms governing the persistence and diurnal cycle of a heavy rainfall corridor. *Journal of the Atmospheric Sciences*, 71(11), 4102–4126. <https://doi.org/10.1175/JAS-D-14-0134.1>
- Tuttle, J. D., & Davis, C. A. (2006). Corridors of warm season precipitation in the Central United States. *Monthly Weather Review*, 134(9), 2297–2317. <https://doi.org/10.1175/MWR3188.1>
- Wallace, J. M. (1975). Diurnal variations in precipitation and thunderstorm frequency over the conterminous United States. *Monthly Weather Review*, 103(5), 406–419. [https://doi.org/10.1175/1520-0493\(1975\)103<0406:DVIPAT>2.0.CO;2](https://doi.org/10.1175/1520-0493(1975)103<0406:DVIPAT>2.0.CO;2)
- Wang, C. C., Chen, G. T. J., & Carbone, R. E. (2004). A climatology of warm-season cloud patterns over East Asia based on GMS infrared brightness temperature observations. *Monthly Weather Review*, 132(7), 1606–1629. [https://doi.org/10.1175/1520-0493\(2004\)132<1606:ACOWCP>2.0.CO;2](https://doi.org/10.1175/1520-0493(2004)132<1606:ACOWCP>2.0.CO;2)
- Wang, W.-C., Gong, W., & Wei, H. (2000). A regional model simulation of the 1991 severe precipitation event over the Yangtze Huai River Valley. Part I: Precipitation and circulation statistics. *Journal of Climate*, 13, 74–92.
- Xu, W., Zipser, E. J., & Liu, C. (2009). Rainfall characteristics and convective properties of Mei-Yu precipitation systems over South China, Taiwan, and the South China Sea. Part I: TRMM Observations. *Monthly Weather Review*, 137, 4261–4275.
- Xu, X., Xue, M., Wang, Y., & Huang, H. (2017). Mechanisms of secondary convection within a mei-yu frontal mesoscale convective system in eastern China. *Journal of Geophysical Research: Atmospheres*, 122, 47–64. <https://doi.org/10.1002/2016JD026017>
- Xue, M. (2016). Preface to the special issue on the “Observation, Prediction and Analysis of severe Convection of China” (OPACC) National “973” Project. *Advances in Atmospheric Sciences*, 33(10), 1099–1101. <https://doi.org/10.1007/s00376-016-0002-3>
- Yang, F., Pan, H.-L., Krueger, S. K., Moorthi, S., & Lord, S. J. (2006). Evaluation of the NCEP global forecast system at the ARM SGP site. *Monthly Weather Review*, 134(12), 3668–3690. <https://doi.org/10.1175/mwr3264.1>
- Yin, S., Chen, D., & Xie, Y. (2009). Diurnal variations of precipitation during the warm season over China. *International Journal of Climatology*, 29, 1154–1170. <https://doi.org/10.1002/joc.1758>
- Yu, R., & Li, J. (2016). Regional characteristics of diurnal peak phases of precipitation over contiguous China (in Chinese with English abstract). *Acta Meteorologica Sinica*, 74, 18–30.
- Yu, R., Li, J., & Chen, H. (2009). Diurnal variation of surface wind over central eastern China. *Climate Dynamics*, 33(7–8), 1089–1097. <https://doi.org/10.1007/s00382-008-0478-3>
- Yu, R., Li, J., Chen, H., & Yuan, W. (2014). Progress in studies of the precipitation diurnal variation over contiguous China (in Chinese with English abstract). *Acta Meteorologica Sinica*, 72, 948–968. <https://doi.org/10.11676/qxb2014.047>
- Yu, R., Xu, Y., Zhou, T., & Li, J. (2007). Relation between rainfall duration and diurnal variation in the warm season precipitation over central eastern China. *Geophysical Research Letters*, 34, L13703. <https://doi.org/10.1029/2007GL030315>
- Yu, R., Zhou, T., Xiong, A., Zhu, Y., & Li, J. (2007). Diurnal variations of summer precipitation over contiguous China. *Geophysical Research Letters*, 34, L01704. <https://doi.org/10.1029/2006GL028129>
- Yuan, W., Yu, R., Zhang, M., Lin, W., Chen, H., & Li, J. (2012). Regimes of diurnal variation of summer rainfall over subtropical East Asia. *Journal of Climate*, 25(9), 3307–3320. <https://doi.org/10.1175/JCLI-D-11-00288.1>
- Zhong, S., Fast, J. D., & Bian, X. (1996). A case study of the Great Plains low-level jet using wind profiler network data and a high-resolution mesoscale model. *Monthly Weather Review*, 124(5), 785–806. [https://doi.org/10.1175/1520-0493\(1996\)124<0785:ACSOTG>2.0.CO;2](https://doi.org/10.1175/1520-0493(1996)124<0785:ACSOTG>2.0.CO;2)
- Zhou, T., Yu, R., Chen, H., Dai, A., & Pan, Y. (2008). Summer precipitation frequency, intensity, and diurnal cycle over China: A comparison of satellite data with rain gauge observations. *Journal of Climate*, 21(16), 3997–4010. <https://doi.org/10.1175/2008JCLI2028.1>
- Zhu, K., Xue, M., Zhou, B., Zhao, K., Sun, Z., Fu, P., et al. (2018). Evaluation of real-time convection-permitting precipitation forecasts in China during the 2013–2014 summer season. *Journal of Geophysical Research: Atmospheres*, 123, 1037–1064. <https://doi.org/10.1002/2017JD027445>